LA-14209-T
Thesis

Effects of Cylindrical Charge Geometry and Secondary Combustion Reactions on the Internal Blast Loading of Reinforced Concrete Structures

Los Alamos
NATIONAL LABORATORY
EST. 1943

The World's Greatest Science Protecting America

This thesis was accepted by the Department of Mechanical Engineering, New Mexico Institute of Mining and Technology, Socorro, New Mexico, in partial fulfillment of the requirements for the degree of Masters of Science in Engineering Mechanics.

LA-14209-T
Issued: May 2005

Effects of Cyclindrical Charge Geometry and Secondary Combustion Reactions on the Internal Blast Loading of Reinforced Concrete Structures

Matthew A. Price

Los Alamos
NATIONAL LABORATORY
EST.1943

The World's Greatest Science Protecting America

ACKNOWLEDGEMENTS

I would like to offer my sincerest thanks to the members of my advisory committee for their assistance with my thesis research and involvement in my education for this degree. I graciously acknowledge Professor Harold Walling for his help in choosing a thesis topic and the guidance that he has given me during my research.

Thanks to Sandy Powell for her work and contributions through the HEET program. Thanks to Daniel Trujillo for his enormous contribution to the JCAT-340 project and constant patience with my questions and problems. Thanks to Ronnie Parker for his concurrent involvement in JCAT-340 test series and his insights in the CTH hydrocode pressure predictions. Thanks to Jason Wilke for his support and advice in calculations and contagious enthusiasm for engineering work.

A special thanks to my family for their praise and encouragement in pursuing this advanced degree.

This work was performed under contract for the Department of Energy

Contract Number: 87083-001-03 4X

LA-14209-T

TABLE OF CONTENTS

LIST OF FIGURES v

LIST OF TABLES viii

LIST OF SYMBOLS AND ABBREVIATIONS ix

1.0 INTRODUCTION 1

2.0 BACKGROUND AND HISTORY 3

2.1 Test Description and Data Acquisition 6

3.0 DETONATION PROCESS AND AIRBLAST FORMATION 11

3.1 Shock Interactions 16

3.2 Scaling Methods 18

4.0 NUMERICAL COMPUTATIONS 21

4.1 Finite-Element Code Methods 23

4.2 AUTODYN Verification: Spherical Airblast Models 25

4.3 Airblasts from Cylindrical Charges 30
4.3.1 Predictive Methods for Cylindrical Charges 33
4.3.2 Analysis of JCAT-340 Charge Geometries 35

5.0 AIRBLAST LOADING OF STRUCTURES 40

5.1 Effect on Structures 41

5.2 Effects of Airblast Confinement 43

6.0 GAS IMPULSE PHASE 45

6.1 Contribution of the Secondary Reactions 46
6.1.1 Detonation Reactions and Product Hierarchy 47
6.1.2 Effects of Confinement 48
6.1.3 Predictions for Fireball Size 49
6.1.3 Predictions for Fireball Duration 52
6.1.4 Separation of Fireball from Shock Boundary 54

6.2 Effects of Thermal Radiation on Measurements 55

7.0 ANALYSIS OF JCAT-340 TEST DATA 57

7.1 Comparison of AUTODYN Models to Test Data 58

7.2 Effects of Charge Height and Presence of Blow-Out Panels 61

7.3 Late-Time Impulse from Secondary Reactions 63

7.4 *Summary of Results 66*
7.4.1 Peak Pressures and Initial Shock Behavior 66
7.4.2 Effects of Secondary Reactions 69

8.0 Additional Comments about jcat-340 Tests 71
8.1 Cylindrical vs. Spherical Charge Geometry Effects 71
8.2 Explosive Charge Density Effects 74
9.0 CONCLUSIONS 77
APPENDIX A 1
APPENDIX B 5
APPENDIX C 9
REFERENCES 16

LIST OF FIGURES

Figure 1: Plan view schematic for Building 340. 4

Figure 2: Set-up for reflected pressure gauges. 8

Figure 3: Typical piezoelectric pressure gauge used for measurements. 9

Figure 4: PBX-9501 P-υ Hugoniots and Raleigh line for the detonation velocity. 15

Figure 5: Reflection factor with angle of incidence for oblique shocks. 17

Figure 6: Typical Mach stem formation from a high-explosive charge. 18

Figure 7: Model set-up for the 2-D spherical validation models. 25

Figure 8: Comparison of AUTODYN spherical charge models to empirical test data. ... 28

Figure 9: Comparison of calculated airblast parameters for 7500-ft elevation. 29

Figure 10: Empirical relationships for cylinders with various L/D ratios at $\theta = 90^{o}$. 31

Figure 11: Air shock formation from a cylindrical charge with L/D = 0.50. 32

Figure 12: Airblast from cylindrical charge with L/D = 0.50 (initiated at $\theta = 180^{o}$). 33

Figure 13: AUTODYN cylinder model for L/D = 1.0 shown directly after remap. 35

Figure 14: Comparison of a cylindrical charge with L/D = 1.0 at Z = 8.04 $ft/lb^{1/3}$. 36

Figure 15: Comparison of a cylindrical charge with L/D = 1.0 at Z = 12.96 $ft/lb^{1/3}$. 37

Figure 16: Peak pressure predictions for L/D = 0.50. 38

Figure 17: Peak pressure predictions for L/D = 1.25. 38

Figure 18: Peak pressure profiles from cylinder with L/D = 1.0. 39

Figure 19: Typical pressure-time curve for a free-air shock. 40

Figure 20: Dynamic magnification factor for a triangular impulse load on a single degree of freedom system. 42
Figure 21: Detonation products of PBX-9501 calculated from chemical equilibrium. 48
Figure 22: Empirical and theoretical predictions of fireball size. 51
Figure 23: Predictions for fireball duration of TNT and PBX-9501 53
Figure 24: Separation of shock front from fireball boundary. 55
Figure 25: AUTODYN 3-D model set-up with gauge locations. 58
Figure 26: Experimental and predicted pressure data comparison for the 25-lb test. 59
Figure 27: Back wall and ceiling pressure data comparison for the 25-lb test. 60
Figure 28: Secondary peak pressures caused by reflecting shocks from 100-lb charge. 61
Figure 29: AUTODYN 3-D model comparison for initial shock. 62
Figure 30: Airblast showing Mach stem formation for the 75-lb AUTODYN model. 63
Figure 31: Pressures up to 300 ms for the 25-lb test. 64
Figure 32: Test video from 5-lb shot showing fireball size. 65
Figure 33: Pressures from 15 ms to 200 ms for the 5-lb shot. 66
Figure 34: Fireball being pushed out of the bay from a large charge size. 69
Figure 35: Impulse distribution contours on bay walls from a cylindrical charge with L/D = 1.0. 72
Figure 36: Difference between charge geometries for the ceiling. 73
Figure 37: Rate stick model for the study of shock transmission between explosives and density effects for PBX-9501 76

Figure A.1: Experimental and predicted pressure data comparison for the 75-lb test..... 10

Figure A.2: Experimental and predicted pressure data comparison for the 5-lb test..... 11

Figure A.3: Experimental and predicted pressure data comparison for the 50-lb test..... 12

Figure A.4: Back wall and ceiling pressure data comparison for the 50-lb test..... 13

Figure A.5: Experimental and predicted pressure data comparison for the 50-lb test..... 14

Figure A.6: Pressures from 10 ms to 300 ms for the 100-lb shot..... 15

LIST OF TABLES

Table 1: Details of the center-bay charge location tests for JCAT-340 7

Table 2: Conservation equations for shock wave and detonation phenomenon. 13

Table 3: Minimum and maximum scaled distances, in units of ft/lb$^{1/3}$ 20

Table 4: AUTODYN spherical charge model results. Model run time was 11 ms. 27

Table 5: Summary of tests analyzed. 57

Table 6: Comparison of positive impulse for gauges in 25-lb test. 60

Table 7: Comparison of peak pressures for the 5-lb tests. 67

Table 8: Comparison of peak pressures for the 25-lb tests. 67

Table 9: Comparison of peak pressures for 50-lb tests. 67

Table 10: Comparison of peak pressures for the 75-lb tests. 68

Table 11: Predictions of fireball duration for JCAT-340 tests. 70

Table A.1: AUTODYN parameters for PBX-9501 (JWL EOS) 3

Table A.2: AUTODYN parameters for air (Ideal Gas EOS) 4

Table A.3: Constituents of PBX-9501 and calculation of the molecular weight. 5

Table A.4: Properties of PBX-9501. 6

Table A.5: Molar heat capacity coefficients for combustion gasses. 8

LIST OF SYMBOLS AND ABBREVIATIONS

a, b, c	Coefficients in molar heat capacity of gasses
c	Local sound speed
d	Typical length of a computational cell
h	Height of charge above sea level
i_g	Gas impulse
k_p	Scaling factor for pressure
k_r	Scaling factor for distance
n	Number of moles of gas
n_{CG}	Number of moles of combustion gasses
n_{DG}	Number of moles of detonation gasses
n_{HE}	Number of moles of high explosive
q	Artificial viscosity
t	Time duration of fireball
t_a	Time of arrival for shock front
t_{d+}	Positive phase duration
t_{d-}	Negative phase duration
u	Velocity in the x-direction
u_0	Initial particle velocity of material
u_1	Particle velocity after interaction
u_{CJ}	Particle velocity at Chapman-Jouget state
x	Component of Cartesian coordinate system

A, B, C	Constant parameters in JWL equation of state
BEC	Blast effects computer
C_0	Bulk sound speed of material
C_L	Linear term for artificial viscosity
C_Q	Quadratic term for artificial viscosity
CFL	Courant-Friedrichs-Lewy condition
CJ	Chapman-Jouguet state
D	Detonation velocity; Fireball diameter
DDESB	Department of Defense Explosives Safety Board
DMF	Dynamic magnification factor
DRI	Denver Research Institute
E	Energy contained in explosive
E_0	Initial internal energy of material
E_1	Internal energy after interaction
E_{CJ}	Internal energy at Chapman-Jouget state
EOS	Equation of State
ESA	Engineering Science and Applications Division
HE	High explosive
HEET	High Explosives Engineering Training program
HSE	(United Kingdom) Health and Safety Laboratory
I	Impulse
JCAT	Joint Characterization and Analytical Tests (of TA-16 Bldg. 340/342)
JWL	Jones-Wilkins-Lee (EOS)

LANL	Los Alamos National Laboratory
LLNL	Lawrence Livermore National Laboratory
M	Explosive or propellant mass
MEE	Materials and Explosives Engineering
MSL	Mean sea level
P	Pressure of gasses
P_0	Initial pressure of material; ambient atmospheric pressure for air
P_1	Pressure after interaction
P_x	Pressure before shock interaction
P_y	Pressure after shock interaction
P_{CJ}	Pressure at Chapman-Jouget state
Q	Chemical energy released by detonation (per unit mass)
R	Gas law constant; Radial distance from charge
R1, R2	Constant parameters in JWL equation of state
S	Coefficient in linear u-U relationship
STP	Standard temperature and pressure
T	Temperature of gas
T_0	Ambient temperature
T_a	Adiabatic flame temperature
T_d	Time duration of vent stage
TMD	Theoretical maximum density
U	Shock velocity
USAE	United States Army Engineers

W	Charge weight — often as TNT equivalence
Z	Shock impedance; Scaled distance
$\alpha, \beta, \theta, \kappa$	Constant parameters in BKW equation of state
β	Angle of incidence of a shock front
ρ_0	Initial density of material
ρ_1	Density after interaction
ρ_{CJ}	Density at Chapman-Jouget state
τ	Natural period of structure
υ, υ_0	Initial specific volume of material
υ_1	Specific volume after interaction
υ_{CJ}	Specific volume at Chapman-Jouget state
γ	Ratio of specific heats for material (adiabatic gamma)
ω	Constant parameters in JWL equation of state
Γ	Dynamic magnification factor
γ, n, T	Parameters in the kinetic equation
ΔH_r	Heat of reaction
ΔH_{AB}	Heat of afterburn, or heat from secondary reactions

ABSTRACT

An understanding of the detonation phenomenon and airblast behavior for cylindrical high-explosive charges is essential in developing predictive capabilities for tests and scenarios involving these charge geometries. Internal tests on reinforced concrete structures allowed for the analysis of cylindrical charges and the effect of secondary reactions occurring in confined structures.

The pressure profiles that occur close to a cylindrical explosive charge are strongly dependent on the length-to-diameter ratio (L/D) of the charge. This study presents a comparison of finite-element code models (i.e., AUTODYN) to empirical methods for predicting airblast behavior from cylindrical charges.

Current finite element analysis (FEA) and blast prediction codes fail to account for the effects of secondary reactions (fireballs) that occur with underoxidized explosives. Theoretical models were developed for TNT and validated against literature. These models were then applied to PBX 9501 for predictions of the spherical fireball diameter and time duration. The following relationships for PBX 9501 were derived from this analysis (units of ft, lb, s).

$$D = 6.76 \times W^{1/3} \qquad \text{and} \qquad t = 0.16 \times W^{1/3}$$

Comparison of centrally located equivalent weight charges using cylindrical and spherical geometries showed that the average impulse on the interior of the structure is ~3%–5% higher for the spherical charge. Circular regions of high impulse that occur along the axial direction of the cylindrical charge must be considered when analyzing structural response.

1.0 INTRODUCTION

The field of high-explosives science is one that demands safety and reliability. Performing operations with high explosives requires the proper safeguards and respect for the sensitive nature of the energetic materials involved. It is very important for a large research organization, such as Los Alamos National Laboratory (LANL), to be able to manufacture and machine high-explosive (HE) components in a safe and effective manner. However, the possibility of an accidental detonation cannot be overlooked, and implementing engineering safeguards can minimize the risk to personnel and structural damage during such an event. Designers must consider these risks when designing a structure that will endure the hazards associated with energetic materials. Most often, these hazards consist of airblast loading, ground-shock effects, and fragment impact. To overcome these risks, typical building designs include earth-covered buildings or aboveground buildings that utilize barricades or venting schemes.[1] The object of this thesis is to predict the transient pressure distribution an accidental detonation of cylindrical explosive charges inside an explosive processing bay creates. These heavily reinforced concrete aboveground buildings have a frangible blow-out wall for venting. The numerical predictions will be compared to test measurements when applicable.

The tests used cylindrical charges of PBX-9501 because of the availability and relative low cost of manufacturing this charge geometry. Unfortunately, the majority of current literature and compiled empirical data for airblast behavior is based on center-initiated spherical explosive charges. Because a spherical charge generates a spherically symmetrical shock wave, the shock characteristics for a known charge weight and explosive become solely a function of the radial distance from the charge. For structural

response analysis, the most important of these blast characteristics are generally the peak pressure (incident and reflected), time of arrival, and impulse. For cylindrical charge geometries, the pressure distribution becomes a function of the explosive's length to diameter ratio (L/D), angle from the axis of the cylinder, and distance from the charge. Additional geometric asymmetries arise if the charge is not center-initiated, which is quite common.

There is an additional need to understand the effects of secondary reactions that occur in an airblast and contribute to the impulse delivered to the structure. The term "secondary reactions," also referred to as the fireball or afterburn effects, describes the turbulent combustion of the detonation products with oxygen present in the air. Many common high explosives, including PBX-9501, are considerably underoxidized so that the products of their detonation are very likely to react with the atmospheric oxygen and liberate additional energy. A comparison of the heat of detonation to the heat of combustion for common explosives reveals the amount of energy released by an explosive can easily be doubled or tripled with the complete combustion of the detonation products. However, factors such as pressure, temperature, and confinement control the extent of these reactions, and the actual energy released is quite different from an ideal combustion. Determining the amount of impulse delivered to a structure from the secondary combustion effects is a secondary objective of this analysis.

2.0 BACKGROUND AND HISTORY

The Materials and Explosives Engineering (MEE) group of the Engineering Science and Applications (ESA) Division currently fabricates high-explosives components at LANL. This group's duties include processing, mixing, casting, pressing, drilling, cutting, and disposing of high-explosive components and energetic materials for research at various areas of the Laboratory and for organizations outside of LANL.[2] In the 1950s, two buildings were constructed at LANL Technical Area 16 (TA-16) to house these operations. These buildings, designated as Buildings 260 and 340/342, were similar in construction, but Building 260 contained twenty-five twelve-ft-high bays, whereas Building 340 (Figure 1) had nine twenty-ft-high bays. They were constructed with thick concrete walls heavily reinforced with steel rebar. Operations utilizing high explosives were carried out in several large bays found in pairs on one side of the building. These bays had two-foot concrete walls on three sides and frangible blow-out panels that made up the remaining wall. The buildings contained several smaller rooms to support the personnel and operations, but this study did not consider them in the analysis and explosive testing of the building.

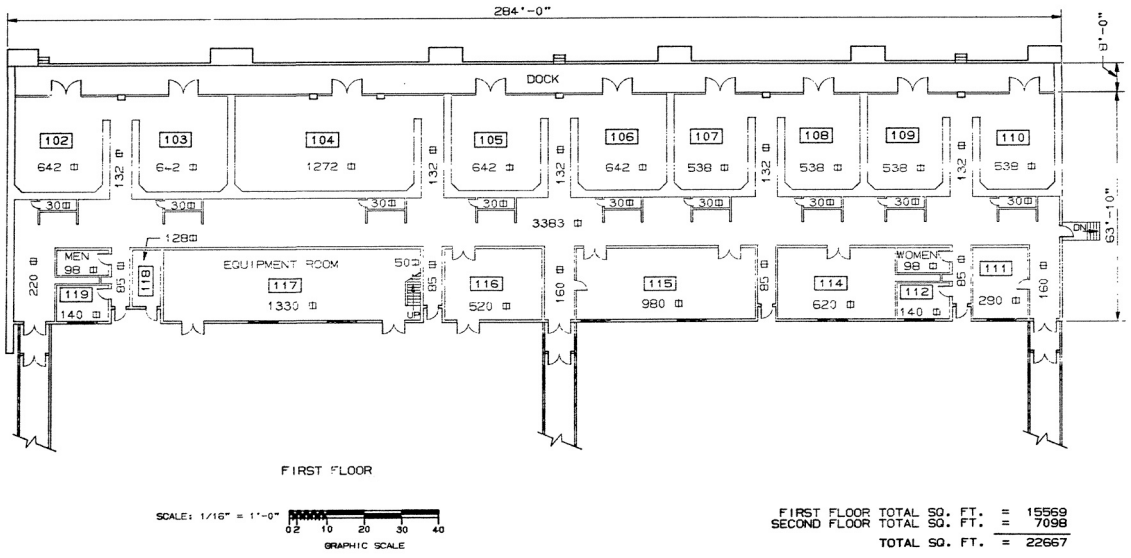

Figure 1: Plan view schematic for Building 340. All bays except 104 were used for JCAT-340.

In 1959, the accidental detonation of approximately seven and a half pounds of PBX 9404 claimed the lives of two workers involved in an explosive drilling operation at Building 260. In response, Charles A. Anderson (1969) built and tested two one-eighth-scale models of a Building 260 bay pair[3] to investigate the accident and prepare a report. He tested the models with hemispherical and cylindrical charges of PBX-9404 with scaled charge weights equivalent to HE charges of 25 to 370 pounds. The charges were placed at a scaled distance of four feet above the floor and at locations that simulated various machining operations. Anderson measured the dynamic strain, incident and reflected pressures and impulse, and the motion of the wall and roof panels. The limits for elastic and plastic behavior of the roof panels were determined based on the deflection and structural damage. Additionally, the tests assessed the potential hazards to personnel from overpressures in the building. Using the scaling laws, the data from these models

could be directly correlated to Building 260 to provide insight into the consequences of an accidental detonation.

Building 340 has historically been a large HE formulation facility, but the fabrication of high-explosive components at LANL has declined in recent years, and the decision was made that this building was no longer necessary. Building 340 was decommissioned and scheduled to be demolished in the summer of 2004. This situation presented an excellent opportunity to perform a series of tests conceptually similar to C. Anderson's but using a full-scale building. Members of the ESA-MEE group proposed and developed these tests, and the project was headed by Daniel Trujillo. The project was called the Joint Characterization and Analytical Tests of TA-16 Building, 340/342, or the JCAT-340 test series. The JCAT-340 tests consisted of detonating charges of PBX-9501 varying from 25 grams to over one hundred pounds at predetermined locations in the bays to investigate both the entire structural response and the response of the frangible blow-out panels. The author's responsibilities for this project consisted of providing calculations and predictions for the pressures and impulses at various target locations that would occur during the blast loading of these bays. This work was conducted as part of the High-Explosives Engineering Training (HEET) program at LANL.[2] This program is aimed at developing young engineers and scientists to transition the intellectual expertise from the previous generation of explosives workers at LANL.

A series of calculations and finite element analysis (FEA) computer models have been developed to predict the airblast loading and structural response of the bays. These predictions are compared with data from the actual tests of Building 340 for validation and to understand the internal blast phenomena that occur during a confined explosion.

Providing an explosive weight-limit certification for the explosive manufacturing and machining bays at TA-16, Building 260, which will be the consolidated site for future ESA-MEE explosive processing operations, is a long-term goal of these tests.

2.1 Test Description and Data Acquisition

The initial test series for JCAT-340 consisted of twenty shots. The first five calibration shots used 25-gram and 55-gram cylindrical charges of PBX-9501. These charge weights were chosen so that the blast loading would not remove or greatly damage the blow-out panels. Having the blow-out panels in place would permit an investigation of the panels' response to the 25-lb and 75-lb charges, which would be located one meter above the floor. This charge height was chosen to represent a realistic machining height and produce a stronger reflected shock and Mach stem from the floor (see Section 3.1). The 25-lb and 75-lb charges removed most of the blow-out panels in the building, and the remaining tests were conducted without the panels. The tests without blow-out panels used charges located two meters above the floor to investigate the structural response of the entire bay.

The smaller charges (25 g, 55 g, and 5 lb) were used in four charge locations. However, charges larger than five pounds used only the center bay and back wall locations. All charges were orientated with the cylinder axis perpendicular to the floor and detonated at the top surface. The analysis presented here will focus only on the measurements from the center-bay charge location because this data is more useful in determining the effects of cylindrical geometry and secondary reaction contributions. The Building 340 bays used for testing were all 27 ft long by 20.5 ft high and had a width of either 20 ft or 24 ft.

Table 1 presents a summary of the charge size, location, and geometry for the tests. The explosive charge weights listed are only approximate; the actual weights calculated from the fabricated geometry and pressed densities were usually slightly lower.

Referenced Charge Weight	Charge Height [m]	Bay Width [ft]	Charge Length [in]	Charge Diameter [in]	L/D	Actual Charge Weight
25 gm	1	24	1	1	1.00	23.6 gm
55 gm	1	24	0.884	1.625	0.54	55.1 gm
5 lb	2	24	5.331	4.25	1.25	5.0 lb
25 lb	1	20	7.25	8	0.91	24.1 lb
50 lb	2	20	6	12	0.50	44.9 lb
75 lb	1	24	9.63	12	0.80	72.1 lb
100 lb	2	24	12	12	1.00	89.9 lb

Table 1: Details of the center-bay charge location tests for JCAT-340.

Each test had 32 data acquisition channels available to record data from incident and reflected pressure gauges or accelerometers. Not every test used all of the channels, but the placement of the gauges inside the bays was consistent between the shots. This analysis was concerned with predicting the reflected pressures on the abutting wall, adjacent wall, back wall, and ceiling center and incident pressures in the hallway and adjacent bay center. The wall gauges were placed at an elevation level with the bottom of the charge. The center ceiling gauge proved to be of particular interest for investigating the cylindrical charge effects.

Installation of the reflected pressure gauges consisted of drilling a hole through the concrete walls and securing a 3/4-in. pipe fitting in the hole with epoxy. A nylon mount between the gauge and pipe fitting acted as a damper to reduce ringing. The gauge and nylon fitting were then threaded into the pipe fitting to be flush with the walls. A thin

sheet (1/3 mil) of aluminized Mylar and a small amount of vacuum grease covered the gauges to mitigate the effects of thermal radiation (Figure 2[4]).

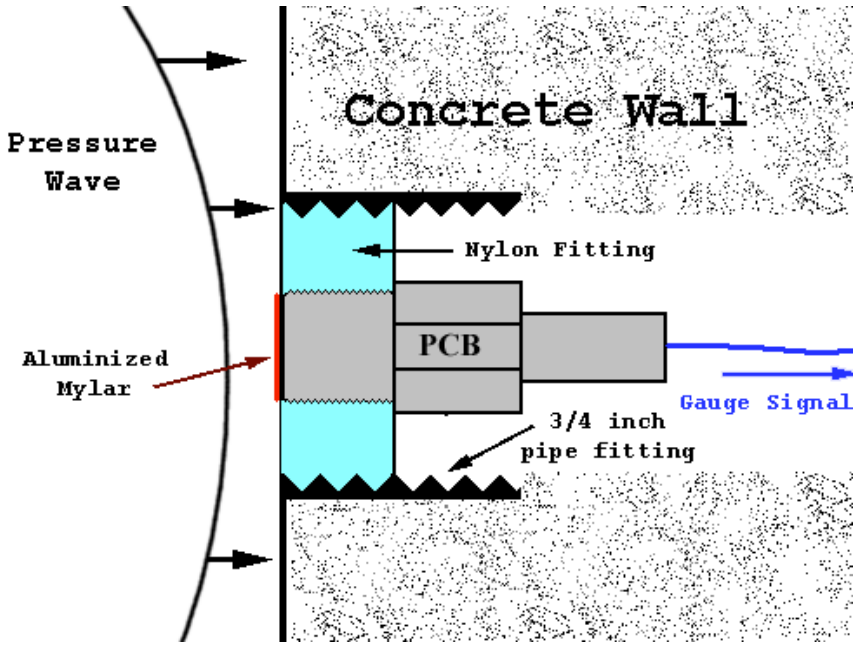

Figure 2: Set-up for reflected pressure gauges.

The incident pressure gauges were mounted in aluminum torpedo tubes and attached so that they were level with the bottom of the explosive charge. These gauges—located in the adjacent bays and bay pairs, the hallways leading out of the bay, outside in front of building, and other locations around the building—measured the attenuation of blast pressures.

The pressure gauges used for both the incident and reflected pressure measurements were piezoelectric type gauges, models PCB Piezotronics 101A, 102A, 102M, 106B, and 112A. They varied in full-scale range from 50 psig to 15000 psig. Figure 3[5] shows a schematic of models 101A and 102A, those most commonly used. These two models are almost identical, but model 102A was designed especially for high-frequency blast and explosion measurements, instead of being a general purpose quartz

gauge. The 112A models are similar but smaller and measured the lower pressures from the 25-g and 55-g calibration shots. The 106B models are high-sensitivity gauges for low-pressure acoustic measurements (i.e., microphone gauges).[6] The pressure measurements were recorded at 200,000 samples per second for 500 ms after detonation. This rate gives a sampling interval of 0.005 ms, which should be adequate for capturing the peak pressures from the airblast shock.

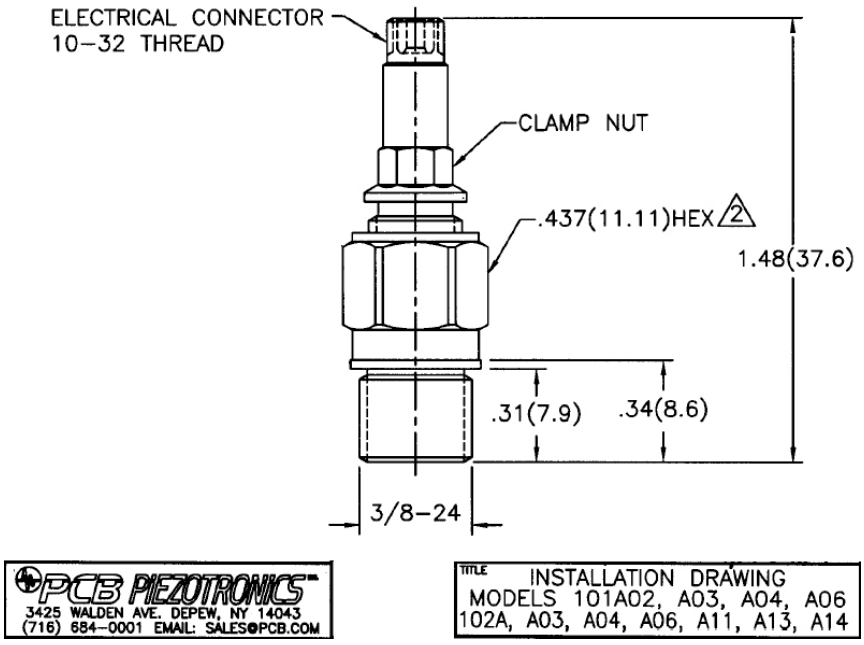

Figure 3: Typical piezolectric pressure gauge used for measurements.[5]

A minimum of 500 ft of cable separated the pressure gauges and the recording instrumentation. A PCB-481 or PCB-584 16-channel signal conditioner converted the high-impedance pressure gauge output to a low-impedance voltage signal. Next, this signal was converted from analog to digital using equipment from National Instruments and recorded electronically as both a binary file and a standard ASCII text file. A primary recording system recorded the data at up to twice the predicted signal amplitude, and a backup system was adjusted to record at four times the predicted signal amplitude.

A HyCam II 16-mm high-speed camera recorded video footage of the tests. The camera was set up at locations specific to each test to capture the features of interest, such as blow-out panel response or shock front and fireball behavior. The speed varied between 100, 300, 1000, 2000, and 3000 frames per second (fps), with the faster frame rates recording the larger charges or capturing dynamic events that occurred more quickly, such as the fireball. In addition to the HyCam, a Canon XL1S digital camera was also used to film the tests. This camera had the capability of recording 680,000 pixels/CCD in three colors at a speed of 30 fps. Accelerometers analyzed the wall and ceiling deflections from the larger charge sizes.

3.0 DETONATION PROCESS AND AIRBLAST FORMATION

An explosive releases the energy it contains as the detonation reaction breaks the chemical bonds in the material and rearranges the atoms to form the reaction products. The initiation process requires a very high activation energy that is usually supplied by a shock wave from a detonator. In comparison to other energetic materials such as propellants, a high-explosive compound generally will not contain as much energy per unit mass. However, it is the rate at which the energy is released that makes the detonation process so unique and remarkable. The solid explosive material is almost instantaneously transformed into gasses at extremely high pressures that drive the shock front.[7] This chemical reaction occurs in a finite thickness of the energetic material called the reaction zone. The point directly behind the reaction at which the explosive material is fully decomposed into the detonation products is known as the Chapman-Jouguet (CJ) state. This point is very important in detonation theory for predicting detonation properties of explosives.

At standard temperature and pressure (STP), the detonation gasses are on the order of 1000–1500 times the original volume of the explosive.[8] As a result, the gasses push outward in a mechanical action that compresses the material in its path. An explosive in contact with another material will send a pressure wave, or shock wave, into the material. If the explosive detonation occurs in air, this shock is referred to as a blast wave, and the process is known as an airblast. The formation of a shock wave is analogous to a snowplow pushing snow on a road. As the snow is pushed, a thickness of

compacted snow builds up. Similarly, an air shock forms after a detonation, but air has no compaction limit, and it can be shocked up to very high peak pressures.

A rarefaction wave that unloads the high-pressure detonation products immediately follows the shock front. This Taylor expansion wave is a function of the isentropic expansion of the gasses, charge size effects, and the degree of confinement.[9] If the products are allowed to expand without interactions, they will decrease in pressure through adiabatic expansion.[10] Alternatively, they may be subjected to increasing pressure from additional shocks or compression waves.

For explosions in air, it is very likely that additional reactions occur behind the shock front as the detonation products react with the oxygen in the air. These secondary reactions release additional energy through a fireball, which a later section will address.

Most mathematical models and hydrocodes assume that the thickness of the detonation front reaction zone is zero, and the shock is treated as a discontinuity or "jump" in material properties. This assumption is necessary to keep the mathematics from becoming complex and is known as the "Simple Theory" of C-J theory. This jump can be described by applying the conservation equations before and after detonation, similar to the mathematical treatment of a shock in a condensed media. These mass, momentum, and energy balance equations are known as the Rankine-Hugoniot jump equations.[9] They are usually developed for shock interactions, but can be applied to a detonation by using the C-J state conditions. Combining these with an Equation of State (EOS) for the detonation products provides mathematical equations that fully describe the detonation process. Table 2 shows the equations of continuity for a shock versus a detonation.

Conservation Equation	Shock Wave	Detonation ($u_o = 0$)
Mass Equation	$\frac{\rho_1}{\rho_0} = \frac{U - u_0}{U - u_1} = \frac{\upsilon_0}{\upsilon_1}$	$\frac{\rho_{CJ}}{\rho_0} = \frac{D}{D - u_{CJ}}$
Momentum Equation	$P_1 - P_0 = \rho_0 (u_1 - u_0)(U - u_0)$	$P_{CJ} = \rho_0 u_{CJ} D$
Energy Equation	$E_1 - E_0 = \frac{1}{2}(P_1 + P_0)(\upsilon_0 - \upsilon_1)$	$E_{CJ} - E_0 = \frac{1}{2}(P_{CJ} + P_0)(\upsilon_0 - \upsilon_{CJ})$

Table 2: Conservation equations for shock wave and detonation phenomena.

There are several ways of presenting these equations graphically. Usually, the pressure, P, is plotted against the particle velocity, u, or specific volume, υ, and the curve is called a *Hugoniot*. The Hugoniot curve represents a locus of all possible final states for the shocked material.[11] Figure 4 presents the P-υ Hugoniot for PBX-9501. Material constants for the unreacted explosive Hugoniot were taken from the LLNL Explosives Handbook, and pressure is found from Equation (3-1), which takes advantage of the linear U-u relationship for most materials:[7,12]

$$P = \frac{C_0^2 (\upsilon_0 - \upsilon)}{\left[\upsilon_0 - S(\upsilon_0 - \upsilon)\right]^2} \qquad (3\text{-}1)$$

Shocks are compressive, so the maximum specific volume the unreacted material can have is the reciprocal of its nominal density ($1/\rho_0$). Similar to the unreacted material, the Hugoniot for the detonation gasses represents the final states possible after the reaction is complete. Usually, this result is very close to the expansion isentrope from the C-J state, and an EOS specific to the explosive usually describes it. Several equations of state for the detonation products of high explosives are usually based on the ideal gas

law. Perhaps the simplest of these comes from applying the ideal gas law to the detonation condition (where gamma is the ratio of specific heats of the gas).[13]

$$P = P_{CJ}\left(\frac{\upsilon_{CJ}}{\upsilon}\right)^{\gamma} \text{ where } \gamma = \frac{C_p}{C_v} \xrightarrow{Detonation} \frac{\upsilon_{CJ}}{\upsilon_0 - \upsilon_{CJ}} \qquad (3\text{-}2;\ 3\text{-}3)$$

However, this equation fails to accurately calculate the pressures at large expansions ($\upsilon >$ 2 cm^3/g).[13] Another EOS commonly used is the Becker-Kistiakowski-Wilson (BKW) equation, which has the following form:[7]

$$P = \rho nRT\left[1 + \rho\kappa\left(T+\theta\right)^{-a}\exp\left(\beta\rho\kappa(T+\theta)^{-a}\right)\right] \qquad (3\text{-}4)$$

Using this equation requires knowledge of the specific volume *and* temperature of the product gasses, which can be difficult to determine because they are codependent. A very common EOS for detonations, and the one used by many current hydrocodes such as AUTODYN, is the Jones-Wilkins-Lee (JWL) form. Appendix A provides the details for this equation of state, which will not be repeated here; the equation has the following form:

$$P = Ae^{-R_1 V/V_0} + Be^{-R_2 V/V_0} + C\left(\frac{V}{V_0}\right)^{-(1+\omega)} \qquad (3\text{-}5)$$

An additional relationship for the detonation products' Hugoniot can be derived by equating the energy described by the gamma law gas EOS to the energy jump equation for the detonation. Respectively, these are given as

$$E = \frac{P\upsilon}{\gamma - 1} \qquad (3\text{-}6)$$

$$E = \frac{1}{2}P\left(\upsilon_0 - \upsilon\right) + Q \qquad (3\text{-}7)$$

Setting these equations equal to each other, the pressure can be solved for in terms of the specific volume. The figure below refers to this as the "Energy Equation."

$$P = Q\left[\frac{2(\gamma-1)}{2\upsilon-(\upsilon_0-\upsilon)(\gamma-1)}\right] \tag{3-8}$$

The Rayleigh line is determined from the conservation of mass and momentum and describes the initial jump path of the detonation or shock. For the detonation condition, it has a slope equal to $-\rho_0^2 D^2$ and passes through the point υ_0. The figure below uses a detonation velocity of 8.80 km/s, which is the value commonly found in literature.[12] The Rayleigh line must be tangent to the Hugoniot for detonation product gasses at the C-J state (shown in Figure 4 for the gamma law EOS). The intersection with the unreacted explosive Hugoniot indicates the von Neumann spike condition. This analysis gives a value of ~52 GPa.

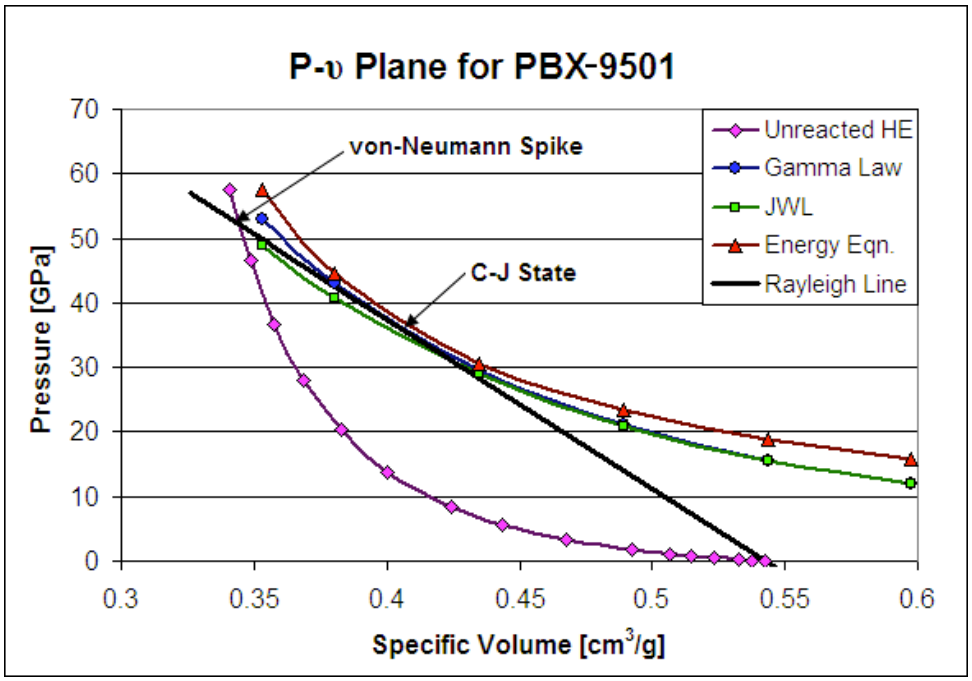

Figure 4: PBX-9501 P-υ Hugoniots and Raleigh line for the detonation velocity.

As the shock travels through the air, it will attenuate by divergence because of the spherical expansion. This attenuation occurs as a cubic function of the radius and accounts for most of the decrease in pressure. A small amount of energy is lost to irreversible processes such as shock heating from mechanical work preformed on the air. Eventually, the shock wave will lose enough energy so that it will start traveling at sonic velocity and be reduced to a sound wave.

3.1 Shock Interactions

When a shock traveling through one material encounters a different material, an interaction occurs at the interface where the shock is partially reflected and transmitted. The difference in shock impedance between the two materials determines the magnitude of these waves. Shock impedance is defined as the product of the material density and the shock velocity, $Z = \rho U$, so the material densities play a large role in the interaction. The density of air is much lower than the density of any other materials that the shock would encounter. Therefore, the reflected pressure is usually much greater than the incident shock. A *normal reflection* is one where the shock encounters a surface head-on. Kinney derives the normal reflection factor as the following:[14]

$$C_r = \frac{(3\gamma - 1)\frac{P_y}{P_x} + (\gamma + 1)}{(\gamma - 1)\frac{P_y}{P_x} + (\gamma + 1)} = \frac{8P_y + 6P_x}{P_y + 6P_x} \qquad (3\text{-}9)$$

The equation on the right side is for the case of strong shocks in air and has a value of $\gamma = 1.4$. This equation has an upper limit of 8.00, which represents the maximum magnification in pressure from reflection.

If the air shock interaction does not occur head on, but at an angle, the process is known as an *oblique reflection*. The reflection factor in this case depends on the amplitude of the incident shock and the angle of the incidence (β). As the incident angle decreases, the reflection factor approaches the case of a normal reflection. The reflection factor goes through a transition where it will increase with increasing angle then decrease as the angle approaches 90°. This transition occurs at larger angles for both strong and weak shocks. For intermediate strength shocks (~30–150 psi), the transition occurs at an angle of approximately 40° as seen in Figure 5.

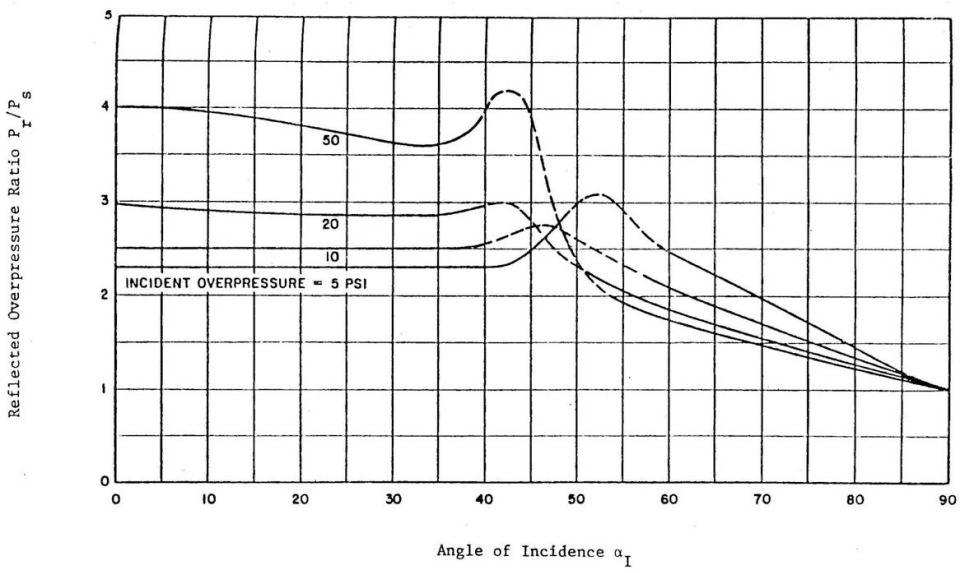

Figure 5: Reflection factor with angle of incidence for oblique shocks.[1]

As an airblast interacts with the ground, it develops both normal and oblique reflections. However, as the angle of incidence exceeds 40°, a plane of pressure forms that propagates normal to the surface. This slightly curved "plane" is known as a *Mach stem* and terminates at the intersection of the incident pressure wave. This point of intersection is called the triple point. Figure 6 illustrates this phenomenon.

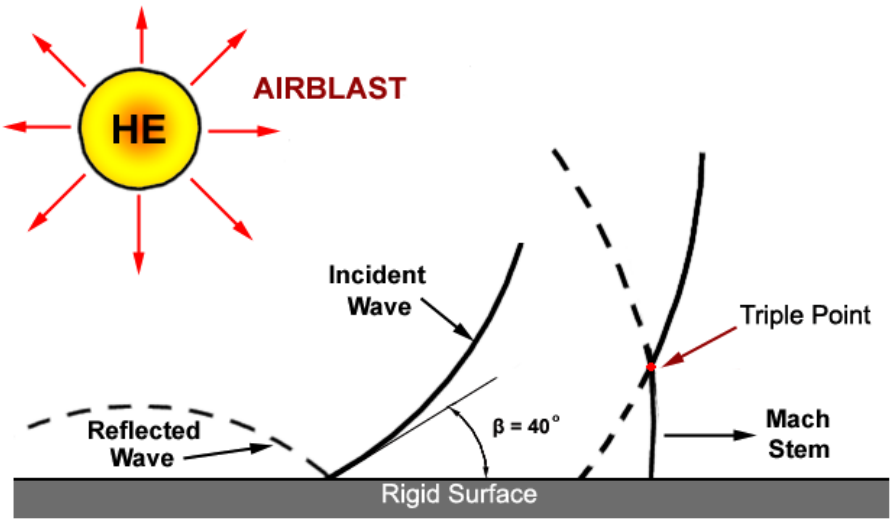

Figure 6: Typical Mach stem formation from a high-explosive charge.

Regions of high reflected pressures, which develop into a full Mach stem, tend to form around the edges of the boundary between an airblast and a surface. These regions are important to confined explosions because of the multiple interactions of the airblast with the structure walls. Mach-stem-like interactions can form regardless of the charge geometry because the airblast from an explosion becomes more spherical as it expands.

3.2 Scaling Methods

Scaling is an important tool for blast calculations because it allows for the comparison of blast characteristics from explosions of different HE charge sizes at different distances. The scaling laws are based on geometric similarity between explosive events.[14] Because an airblast expands spherically in air, the ratio of volumes between two explosions is related to the cubic radius term of the volume of a sphere.

A common practice is to present blast data as a function of scaled distance because this pseudodimensionless term can account for differences in charge size. The formula for scaled distance is given by the following:

$$Z = R/W^{1/3} \quad \text{or} \quad Z = R/E^{1/3} \tag{3-10}$$

Scaled distance is generally expressed in units of [$m/kg^{1/3}$] or [$ft/lb^{1/3}$]. If the charge weight is used instead of the energy contained in the explosive, then it is usually expressed as an equivalent weight of TNT. B. Hopkinson developed this scaling in 1915, and it is often referred to as Hopkinson, or "cube root," scaling.[15] It is also possible to include scaling factors for the atmospheric conditions such as pressure, temperature, density, or sound speed. The most common of these scaling theories is Sach's scaling (1944). Sperrazza (1963) conducted a dimensional analysis and derivation of Sach's scaling law, which is outlined in Baker and results in the following scaling factors for pressure and distance:

$$k_p = \frac{p_0^{(h)}}{p_0^{(0)}} \quad \text{and} \quad k_R = \left(\frac{\frac{E^{(h)}}{E^{(0)}}}{\frac{\rho_0^{(h)}}{\rho_0^{(0)}}} \right)^{1/3} \tag{3-11; 3-12}$$

The dimensionless pressure and distance defined as $k_p = \frac{p^{(h)}}{p^{(0)}}$ and $k_R = \frac{R^{(h)}}{R^{(0)}}$. These equations can be reduced to the more familiar form such as that found in Kinney:[14]

$$\text{scaled distance} = \frac{R(\rho/\rho_0)^{1/3}}{(W/W_0)^{1/3}} \tag{3-13}$$

The subscript "$_0$" denotes the reference conditions. This form can be further reduced using the ideal gas law to express the density in terms of pressure and temperature. Empirical blast data is usually scaled to atmospheric conditions at mean sea level (MSL); however, the JCAT-340 tests were carried out at an altitude of approximately 7500 feet above sea level. To accommodate this difference in altitude requires the use of the scaling formulas for comparison to empirical data from literature (at MSL). Thus, this paper

follows the convention of presenting data as a function of scaled distance given by Equations (3-10) and (3-13). Table 3 gives maximum and minimum values of scaled distance from the charge center to the bay walls for each test. Neglecting the distance to the floor surface, the minimum scaled distance (Z_{min}) is found as the distance to either the abutting or adjacent walls, and Z_{max} corresponds to the diagonal distance to the ceiling corners. The scaled distance to the ceiling center is also of importance and appears in the third column. These distances will be useful later in determining the constraints of the empirical relationships for pressure predictions.

Charge Weight [lb]	$Z_{min\ (Wall)}$	$Z_{max\ (Corner)}$	$Z_{(Ceiling\ Center)}$
0.055	30.86	63.03	44.39
0.121	23.27	48.46	33.46
5	6.73	12.82	7.84
25	3.32	7.91	5.73
50	2.70	5.70	3.77
75	2.77	5.69	3.98
100	2.57	4.72	3.00
300	1.43	3.13	2.04

Table 3: Minimum and maximum scaled distances, in units of ft/lb$^{1/3}$, for each charge size test.

4.0 NUMERICAL COMPUTATIONS

The analysis of the JCAT-340 project used several software tools. The majority of these were applications that provide calculations for airblast scenarios based on empirical data and include BlastX, ConWep, DDESB-BEC, and codes the author wrote in MatLab based on TR-02555. A technical report, written by Kingery and Bulmash, is a very useful reference because it presents a compilation of empirical data from spherical and hemispherical TNT and Pentolite charges.[16] Additionally, it gives polynomial fit equations for blast parameters from TNT charges at sea level atmospheric conditions, which can be scaled for a specific charge size or altitude. Other programs such as AUTODYN and CHEETAH provided a finite-element approach to airblast behavior or an understanding of the chemical kinetics related to the detonation and combustion processes.

BlastX is a program for predicting pressures and impulse from "multiple explosions inside or outside of multiple room structures with shock propagation and venting between rooms."[17] BlastX calculates shock loading as well as the gas impulse for confined explosions. Charges can be of spherical and cylindrical geometry, but cylindrical charges based on the empirical data have some limitations (e.g., pressure predictions in the axial direction tend to be inaccurate). The program offers several types of explosives, but PBX-9501 is not included. However, the user can choose TNT as the HE and use an appropriate TNT equivalency factor for other explosives. BlastX calculations are performed using a series of "rays" that travel from the detonation point

and interact with the defined structure. It also allows the user to change the ambient atmospheric conditions.

The U.S. Army Engineers Research and Development Center developed ConWep, an interactive code for predicting effects such as airblast, penetration, cratering, and ground shock.[18] This program was predominantly used for airblast predictions, but does offer structural calculations for internal blasts and airblast loading of slabs that could be applicable to this project. The code uses predictions from the TR-02555 manual for spherical and hemispherical charges and assumes an exponential decay of pressure with time. It can calculate gas pressure for internal explosions based solely on the charge size, room volume, and venting area.

The Department of Defense Explosives Safety Board (DDESB) has developed a program written in Microsoft Excel for calculating airblast parameters for several types of explosives, cased or uncased, based on equivalent hemispherical charges.[19] This code, the Blast Effects Computer (BEC), uses equations from the TR-02555 for airblast parameters as well as predictions for damage to human organs and probability of window breakage.

AUTODYN is a commercial finite-element hydrocode developed by Century Dynamics Incorporated that is capable of calculations in two and three dimensions using Lagrange, Eulerian, and mixed Lagrangian/Eulerian computational techniques. This program has had a primary role in the computations performed for the JCAT-340 project. In the spring of 2004, the Mechanical Engineering department purchased a full educational copy of AUTODYN, which offered significant improvements over previous versions. The capability of Lagrangian-Eulerian interactions in a three-dimensional (3-D)

model was particularly important. This capability allowed for detonation/airblast calculations and structural response in the same model, which was ideal for models of the JCAT-340 tests.

Codes written in MatLab and Microsoft Excel make simple blast calculations, such as reflected pressure, impulse, and time of arrival. These codes are usable only when the effects of oblique shocks are not a concern. They are applicable to the bay-centered charge tests, because all of the reflected gauges are in the plane of the explosive. For simple blast loading of a rectangular surface, ConWep's "slab loading" feature includes the effects of oblique shocks.

4.1 Finite-Element Code Methods

Because most mathematical models treat a shock wave as a discontinuity, certain problems arise in the dealing with shock propagation in finite element modeling. To handle this, current hydrocodes introduce a numerical factor which "smoothes" the pressure discontinuity over several computational cells. This method of artificial viscosity was first proposed for use in hydrocodes by von Neumann and Richtmyer in 1949.[20] Although the original proposal included only a quadratic term, AUTODYN, like most modern hydrocodes, uses an additional linear term so the complete viscosity correction has the following form:[7]

$$q = -\left[\frac{(c_Q \Delta x)^2}{\upsilon}\frac{\partial u}{\partial x}\left|\frac{\partial u}{\partial x}\right| + \frac{c_L \Delta x}{\upsilon}\frac{\partial u}{\partial x}\right] \qquad (4\text{-}1)$$

The equation implemented in AUTODYN is slightly different in that it uses the specific volume change, $\dot{V}/V$, instead of the differential $\partial u/\partial x$ term.[10] Because q has the

same units of pressure, it is simply added to the pressure term to spread any spikes out over several (generally 3 to 5) computational cells.[7]

Getting a reasonable approximation of the true solution requires a maximum time step for each finite element calculation. AUTODYN uses several parameters in determining the time step to ensure stability of the calculation. The local subgrid time step is found from a minimum of individual time steps, and an additional safety factor is employed (default of 2/3).[10] First, the time step must satisfy the Courant-Friedrichs-Lewy (CFL) condition, which is used to "ensure a disturbance does not propagate across a zone in a single time step."[10]

$$\Delta t_1 \le \frac{d}{c} \tag{4-2}$$

The pseudoviscous terms create further restrictions on the time step. Von Neumann and Richtmeyer showed that the linear C_L and quadratic C_Q terms require respective stability conditions of the following:[20]

$$\Delta t_2 \le \left[4C_Q^2 \left| \frac{\dot{V}}{V} \right| \right]^{-1} \quad \text{and} \quad \Delta t_3 \le \frac{d}{2C_L c} \tag{4-3; 4-4}$$

This calculation reveals that for large discontinuities, i.e., large artificial viscosity terms, the time step decreases. The minimum time step from these conditions is chosen for the calculation.

Finite-element modeling requires several constitutive relationships or equations of state, failure models, and strength models to describe the materials used in a problem. Because the focus of this thesis is airblast behavior, the only materials of concern are air and high explosives. An ideal gas equation of state describes the air and the expanded

detonation products, whereas a JWL EOS describes the unreacted explosive material and initial detonation gases. Appendix A provides more detail.

4.2 AUTODYN Verification: Spherical Airblast Models

A series of spherical blast models were run to validate the accuracy of the AUTODYN finite-element code for airblast calculations. The results were compared with literature sources such as the TR-02555 and ConWep. The DDESB-BEC was not used because it is based on hemispherical charges. The models used a one-kilogram charge of TNT for simplicity. Models were run for atmospheric conditions at both MSL and the elevation of LANL (7500 ft). These models were also used to investigate the effect of cell size on the finite-element calculation by varying the number of computational cells from 31,250 to 980,000.

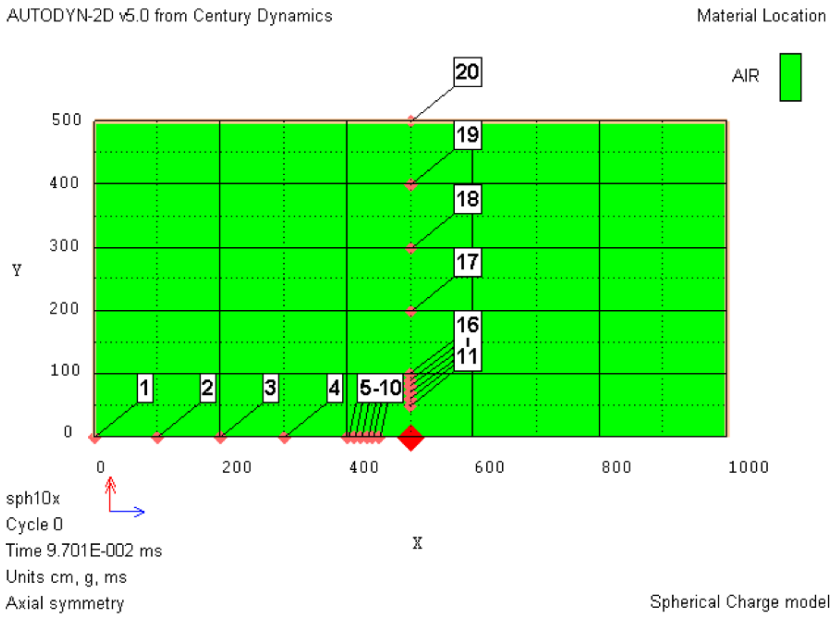

Figure 7: Model set-up for the 2-D spherical validation models.

Figure 7 shows the gauge points, axis labels, and charge location (centered at x=500, y=0 and denoted by the largest diamond marker). This model is symmetric about

the x-axis. To increase accuracy for this spherically symmetric charge, a 1-D "wedge" subgrid was used for the calculation of the first 40 cm of detonation product expansion and then remapped into the 2-D model. See Appendix A for details on the remap process. Gauge locations were set up every 10 cm from 50 cm to 100 cm and every meter from a 1-m to 5-m radial distance from the charge center. Gauge points located along both the x-axis and y-axis investigated the inaccuracies that resulted from spherical shock propagation through rectangular cells and computational errors along the symmetry axis. The models were run out to eleven milliseconds at which point the shock front had traveled beyond all of the gauge points.

Section 3.0 showed that AUTODYN introduces artificial viscosity terms to computationally manage the discontinuity of a shock wave. In effect, this reduces the peak pressures from an airblast as a direct consequence of spreading the shock front across a number of cells. This effect can present problems, and the users of such finite-element codes must determine the optimal cell size for their models.

One approach to determining the ideal cell size for an accurate computation is to run successive models with increasingly smaller cell sizes until the results between models start to converge. Ideally, the model results should approach experimental values. However, a small change in cell size can result in a large increase in the number of cells required, which greatly effects the computational time [see Equations (4-2) and (4-4)].

Number of Cells (Thousands)	Subgrid Cell Divisions	Max Deviation between x and y axis gauges	Actual Computation Time [min]
31.25	250 x 125	2.9%	6
61.25	350 x 175	1.2%	14
125	500 x 250	2.2%	47
245	700 x 350	0.8%	278
500	1000 x 500	1.1%	590
980	1400 x 700	0.4%	980

Table 4: AUTODYN spherical charge model results. Model run time was 11 ms.

Table 4 shows a partial summary of the results from these spherical charge models. Note the trends among alternating models. For example, models for 31.25-k, 125-k, and 500-k cells share similarities because the actual target locations differ slightly from the way the zoning divides the subgrid into cells. It was found that the pressures along the x-axis were almost always lower than the y-axis values. The maximum percent deviation for pressures along the x- and y-axes is shown above with respect to an average of the pressure values.

In many cases, the computational power available limits the modeler. The most computationally intensive model had 980,000 cells and took over 16 hours to run. The time required for each computation dropped off rapidly with the decrease in number of cells. Five more validation models were run with each successive model using approximately half the number of cells of its predecessor. An average of the peak pressure values from the x-axis and y-axis gauge arrays was used to test for convergence. The percentage error deviation of these models from the data presented in TR-02555 was found and is presented below. The legend in Figure 8 shows the number (in thousands) of cells used in the models.

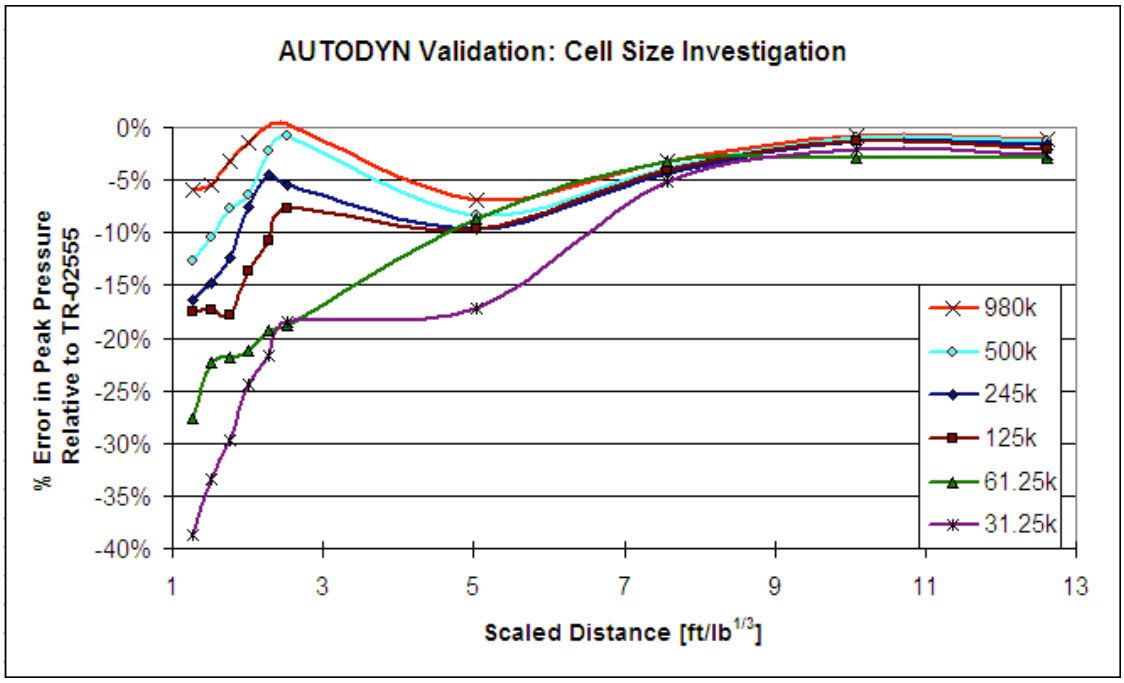

Figure 8: Comparison of AUTODYN spherical charge models to empirical test data.

All of the models seem to converge to published values of peak incident pressure at large distances. The percent error for all but one of the models was within 10% and at a scaled range of 5 ft/lb$^{1/3}$ and within 5% at a scaled range of 8 ft/lb$^{1/3}$. These results are for spherical charges and cannot be directly applied to the JCAT-340 tests. However, the range of scaled distances for the gauges in the 5-lb to 100-lb shots is approximately $1.4<Z<13$ ft/lb$^{1/3}$, so the error from large cell sizes should be minimal in the AUTODYN models. The errors that arise between the 500-k, 245-k, and 125-k models are relatively small and not worth the extra calculation time and computer resources required. The model containing 245,000 cells appeared to be optimal for this particular problem.

Even though the cell size can make quite a difference in the calculated peak pressure values, the impulse should not be reduced because of the artificial viscosity terms. A comparison of the impulses over 11 ms for the spherical validation models showed a deviation of less than 1% between all the models.

An additional model was run to investigate the effect of atmospheric conditions at the elevation of the JCAT-340 test site (7500 ft). Figure 9 presents a comparison of the values of peak pressure and arrival time for the detonation of a 1-kg TNT sphere. Values for peak pressure and arrival time were calculated from TR-02555, ConWep, and an AUTODYN model containing 980,000 cells.

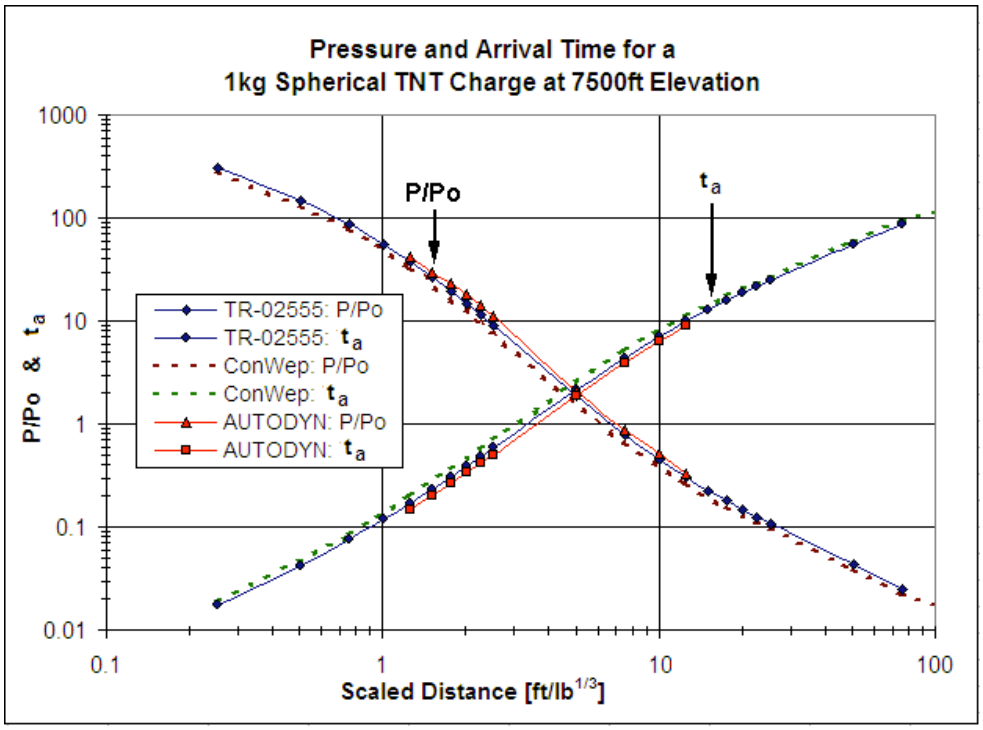

Figure 9: Comparison of calculated airblast parameters for 7500-ft elevation.

The pressure is expressed as the ratio of peak pressure to the ambient pressure, and arrival time is expressed in units of milliseconds. Arrival time and the pressure ratio use the same axis scale. Using the TR-02555 data as the "correct" values, ConWep underpredicted the peak pressure by an average of 13% and overpredicted the arrival time by 12%. An identical calculation for pressures and arrival times at MSL showed essentially no deviation between ConWep and TR-02555. The AUTODYN 2-D model was on the other side of the prediction and gave peak pressures that are high by 15% and

arrival times that are lower by 12%. This spread in predictions is relatively large, especially when the spherical airblast is the most well understood of all charge geometries.

4.3 Airblasts from Cylindrical Charges

The detonation product gas expansion process for a cylindrical charge is significantly more complex than its spherical counterpart and is dependent on several factors. The most important of these are the length-to-diameter ratio (L/D) and point of detonation. As L/D increases, the shock wave profile approaches that of a string (e.g., detcord). Alternatively, as L/D approaches zero, the wave profile approaches that of a planar explosion (e.g., thin sheet). However, the charges used for JCAT-340 restricted our range of interest to $0.50<L/D<1.25$ (see Table 1 for the specific ratios). An L/D of one represents the airblast behavior closest to a spherical charge. Figure 10 shows that this is particularly evident at scaled distances greater than 10 $ft/lb^{1/3}$ for gauges perpendicular to the charge axis (i.e., $\theta = 90^{o}$).[1]

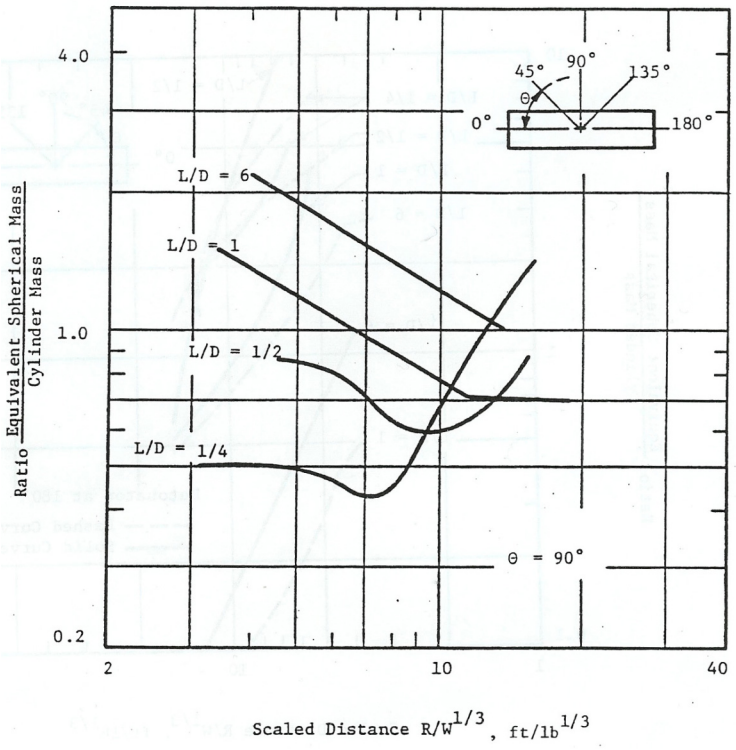

Figure 10: Empirical relationships for cylinders with various L/D ratios at θ = 90°.[1]

An SE-1 detonator at one end initiated the cylindrical charges used [for JCAT-340]. As the detonation front travels down the length of the charge, a conical air shock forms along the cylinder. The detonation wave then reflects off the free surface at the bottom end ($\theta = 0^o$) of the explosive and drives the detonation products in that direction. As a result, the pressures at this end of the cylinder are initially higher than at other locations. As the detonation products expand into the air, a symmetric oblong bell shape pressure wave forms (Figure 11). Eventually this shape becomes more spherical, but this initial shape is very influential on the pressure distribution of the air shock found close in to the charge.

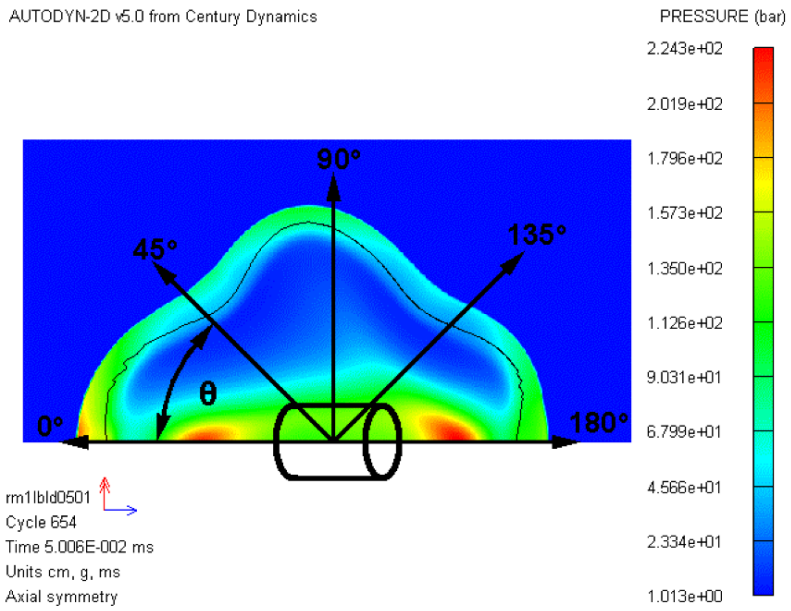

Figure 11: Air shock formation from a cylindrical charge with L/D = 0.50, initiated at θ = 180°.

The cylinder detonation shown above includes a depiction of the original cylinder and the definition of the angle theta (θ). Using this convention, adopted from TIC-11268, theta is the angle measured from the axis of the cylinder, and detonation occurs at θ = 180°.[1] Similar to a spherical charge airblast, the detonation shock reflects off the free surfaces of the explosive to form a secondary shock front. The pressures in this shock wave are significantly lower but can usually be seen in a pressure-time history. Another characteristic of a cylindrical detonation is the separate shocks that form off the end faces of the cylinder. These shocks are a result of interference from the detonation waves off the different faces of the explosive and are commonly referred to as "bridge waves" and shown in Figure 12.[1] The size and angle of these secondary shocks are a function of the L/D ratio, but these eccentricities become less noticeable with airblast expansion. Notice that the shock thickness, and thus impulse, also changes with the angle around the charge.

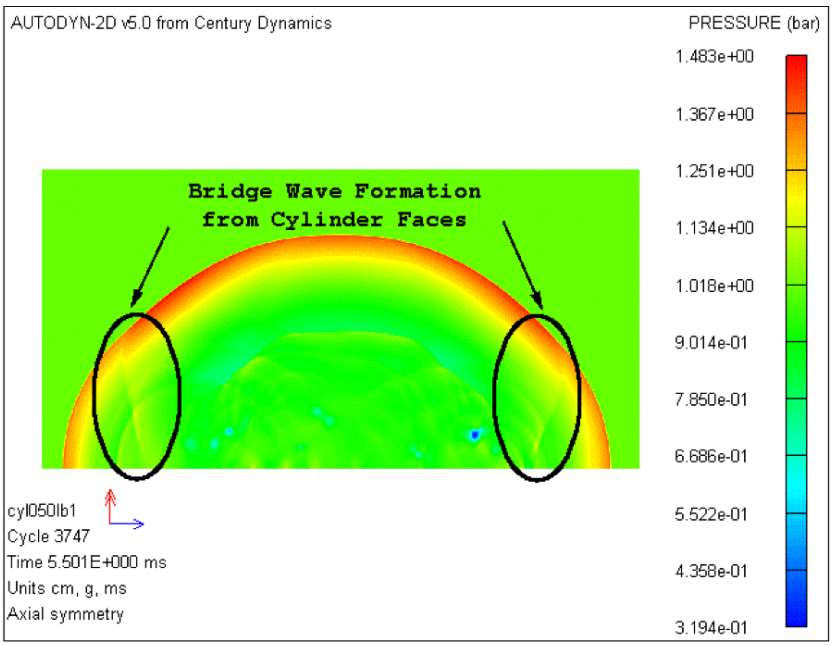

Figure 12: Airblast from cylindrical charge with L/D = 0.50 (initiated at $\theta = 180^{o}$).

4.3.1 PREDICTIVE METHODS FOR CYLINDRICAL CHARGES

Published data for cylindrical charges is very scarce. Tests performed by Wisotski and Snyer at the Denver Research Institute (DRI) provided a primary source for compiled test data from cylindrical charge geometries.[1] However, this data is limited to predictions for peak pressure from charges of $0.25<L/D<10$ at scaled distances of approximately $5<Z<20$ ft/lb$^{1/3}$. Curve-fit equations from the data are presented for peak pressure from TNT charges at sea level. Functions for the predictions of charges with $L/D < 1$ and $L/D \geq 1$ are given in terms of Z, L/D, and θ.[1]

$$y = \begin{bmatrix} 2.0467 - 0.1146X + (0.1285 - 0.0342X)\cos\theta \\ +(0.0621 - 0.3280X)\cos 2\theta + (-0.0029 + 0.0304X\cos 3\theta \\ +(-0.1532 - 0.998X)\cos 4\theta \end{bmatrix}$$

$$+\begin{bmatrix} -2.1617 + 0.1422 + (-0.2079 + 0.1161X)\cos\theta \\ +(-0.4178 + 0.3686X)\cos 2\theta + (-0.1372 + 0.0648)\cos 3\theta \\ +(-0.3484 + 0.1191)\cos 4\theta \end{bmatrix}\lambda \text{ for L/D } \geq 1.0 \quad (4\text{-}5)$$

$$+\begin{bmatrix} 0.4366 + 0.0418X + (0.0138 + 0.0983X)\cos\theta \\ +(0.1178 + 0.1451X)\cos 2\theta + (0.2556 - 0.043X)\cos 3\theta \\ +(0.3123 + 0.1616X)\cos 4\theta \end{bmatrix}\lambda^2$$

$$y = \begin{bmatrix} 2.0467 - 0.1753X + (0.1285 + 0.0728X)\cos\theta \\ +(0.0621 - 0.2503X)\cos 2\theta + (-0.0029 + 0.0079X)\cos 3\theta \\ -0.1534\cos 4\theta \end{bmatrix}$$

$$+\begin{bmatrix} -2.1616 + 0.0464 + (-0.2079 - 0.2174X)\cos\theta \\ +(-0.4178 + 0.3426X)\cos 2\theta + (-0.1372 + 0.1171)\cos 3\theta \\ +(-0.3484 - 0.3449)\cos 4\theta \end{bmatrix}\lambda \text{ for L/D } < 1.0 \qquad (4\text{-}6)$$

$$+\begin{bmatrix} 0.4366 + 0.0053X + (0.0138 + 0.0006X)\cos\theta \\ +(0.1178 - 0.2656X)\cos 2\theta + (0.2556 + 0.2072X)\cos 3\theta \\ +(0.3123 - 0.2140X)\cos 4\theta \end{bmatrix}\lambda^2$$

$$X = 1\text{n}\left(L/D\right)$$

$$\lambda = 1\text{n}\left(0.0893 R/W^{1/3}\right) \qquad (4\text{-}7;\ 4\text{-}8;\ 4\text{-}9)$$

$$P_s = 1.22e^{\gamma}$$

BlastX is capable of airblast predictions using two sources of cylindrical data. The first is a calculation for a "Low Height of Burst" explosive that is based on empirical data. This calculation can be used for cylindrical charges that are end-detonated with the axis parallel to the ground at a charge centerline elevation between 0.239 and 0.306 ft/lb$^{1/3}$.[17] A charge located 1 m above the ground would require a charge size of greater

than 1200 lb. Therefore, this data is out of the range of the JCAT-340 tests and cannot be used. The second option in BlastX is to use "Tabular Cylindrical" data, which is based on calculations using the RAGE hydrocode.[18] However, this option is only recommended for larger charge sizes because the program overestimates the peak pressures for smaller charges. The explosive charges are also limited to L/D ratios between 1.0 and 8.0 for the explosive C-4, so only an L/D of 1.0 could be used because it falls within the JCAT-340 range.

4.3.2 Analysis of JCAT-340 Charge Geometries

Cylindrical charge geometries with an L/D of 0.5, 1.0, and 1.25 were analyzed to provide estimates of the effectiveness of the AUTODYN models that later model the JCAT-340 tests. *All charges used in the JCAT-340 tests were end-initiated at* $\theta = 180^{o}$. These models used 998,000 computational cells with an initial detonation computation that was remapped from a smaller subgrid.

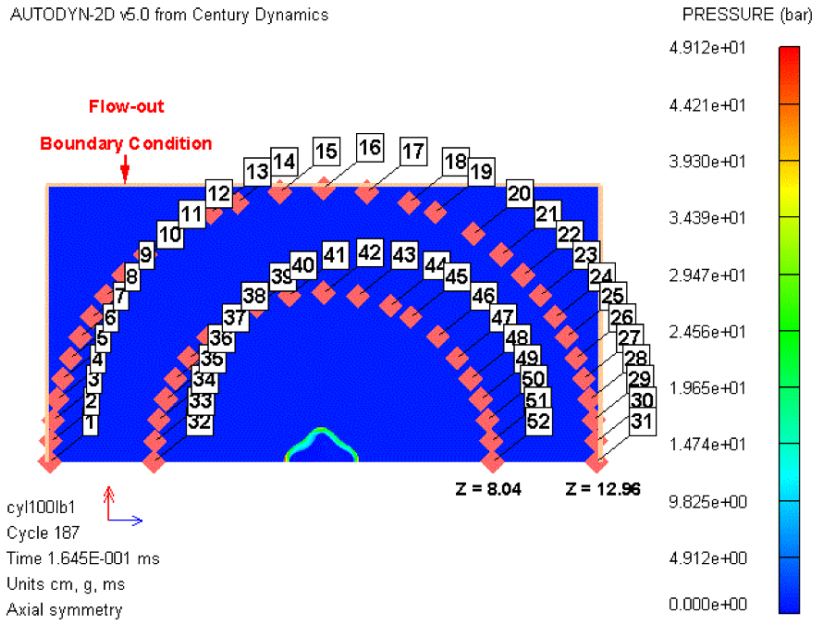

Figure 13: AUTODYN cylinder model for L/D = 1.0 shown directly after remap.

Figure 13 shows the 2-D AUTODYN model that determined the peak pressures around a cylindrical charge of TNT with L/D of 1.0. The pressure data obtained was compared against BlastX and the DRI curve-fit equations (see below). Two arrays of targets were set up at equal distances around the explosive charge at distances of 8.04 and 12.96 ft/lb$^{1/3}$ as shown. The BlastX models used targets at identical locations and a charge of C-4 equivalent to 1 lb of TNT (equivalency factor = 1.129).

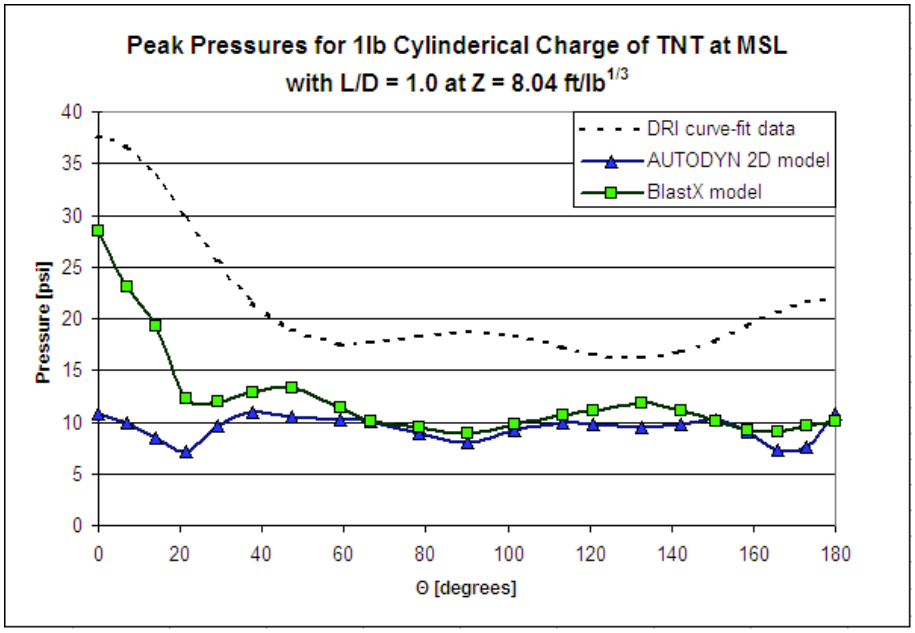

Figure 14: Comparison of a cylindrical charge with L/D = 1.0 at Z = 8.04 ft/lb$^{1/3}$.

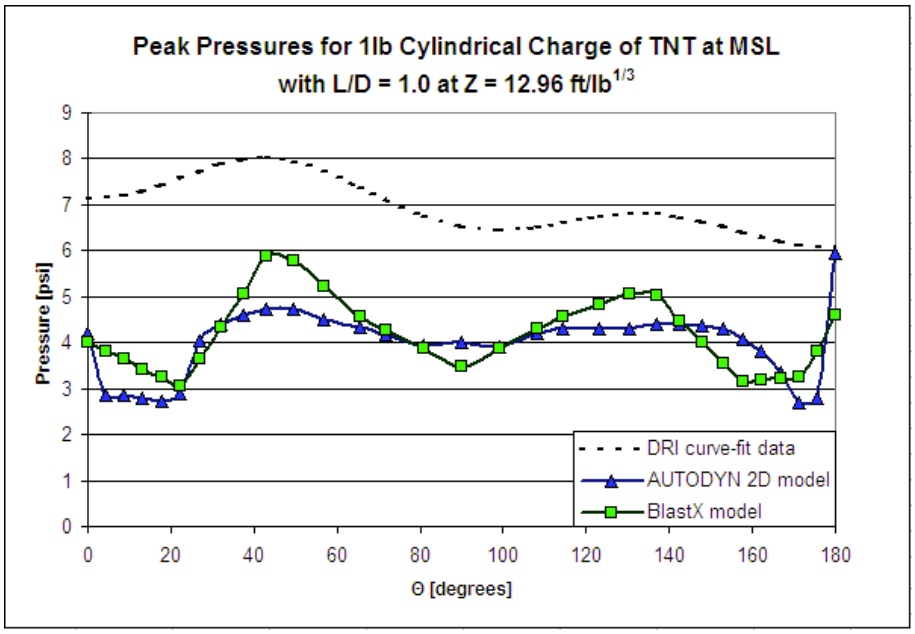

Figure 15: Comparison of a cylindrical charge with L/D = 1.0 at Z = 12.96 ft/lb$^{1/3}$.

As seen in Figures 14 and 15, the peak pressure calculated from AUTODYN and BlastX are moderately close and have similar pressure profiles. At close distances, BlastX predicts a much higher pressure on the end opposite the detonator ($\theta = 0^o$). According to the AUTODYN models, the gauge at this end also recorded the lowest arrival times. High pressures are recorded around the ends of the cylinder ($\theta = 0^o$ and 180^o) because of the formation of bridge waves (see Figure 12). As the airblast expands, these secondary shocks catch up and combine with the primary shock front. The DRI data is significantly higher than the other two methods. This data was originally collected for Comp-B explosive at an atmospheric pressure of 12.03.[1] It was later scaled to TNT at MSL, which introduces the possibility of error. It was necessary to use scaled distances that were quite high to fit the range of the DRI data. However, these values of Z are only seen in charge sizes of five pounds or smaller.

Additional models were run for comparison of AUTODYN and DRI peak pressures predictions for charges with L/D ratios of 0.5 and 1.25 (Figures 16 and 17). It was not possible to use BlastX for calculations of this L/D ratio, and the DRI data is quite a bit higher that AUTODYN especially at lower scaled distances.

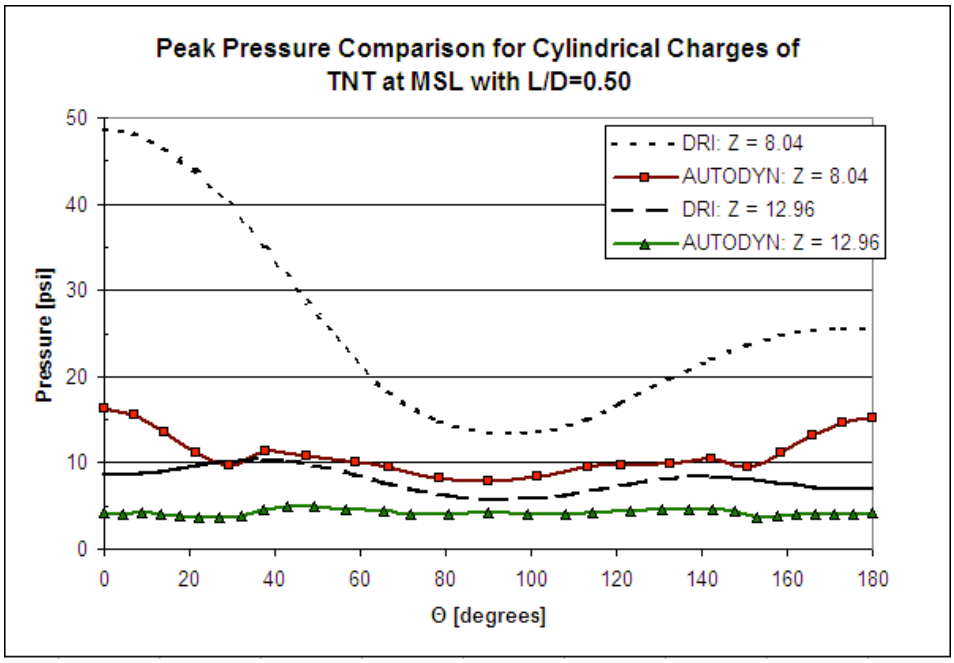

Figure 16: Peak pressure predictions for L/D = 0.50.

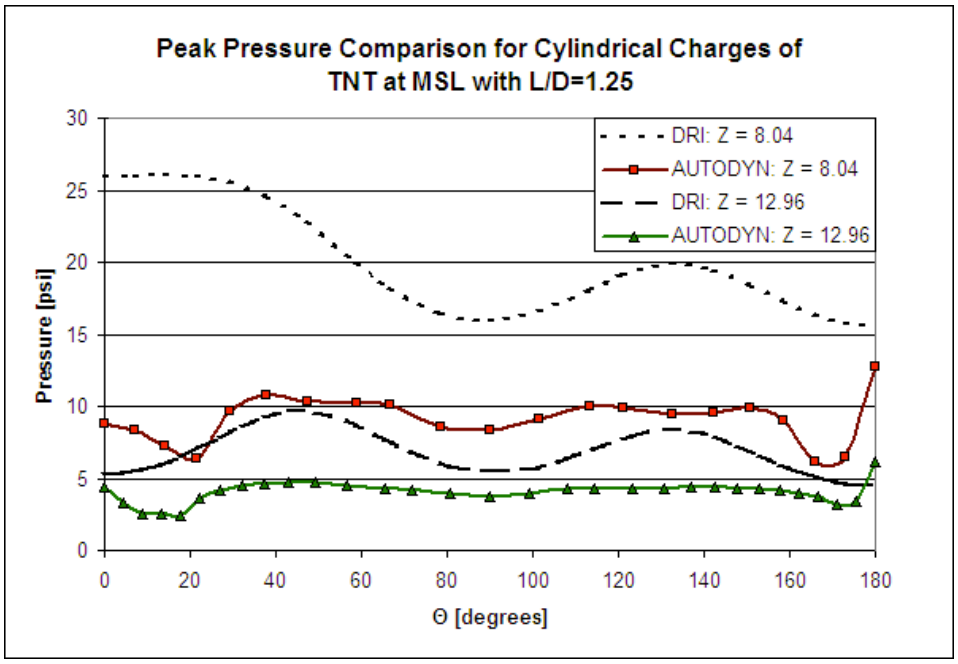

Figure 17: Peak pressure predictions for L/D = 1.25.

Observe that, as the scaled distance increases (i.e., shock front becomes spherical), the variation in the pressure profiles decreases and the predictions from the DRI and AUTODYN data tend to converge. The decrease in variation through the pressure profile with increasing scaled distance can be seen in greater detail in the following figure (Figure 18) taken from TIC-1126.

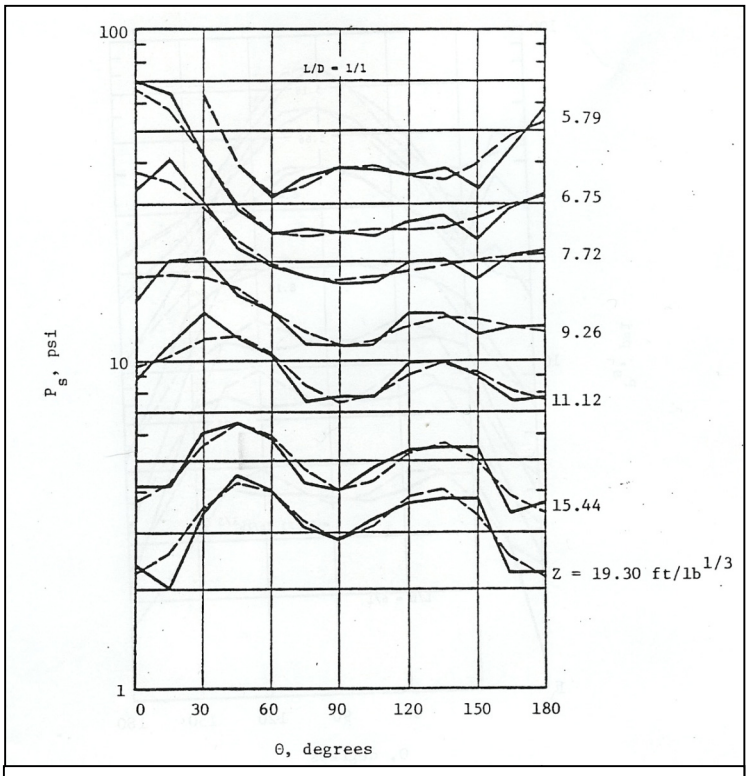

Figure 18: Peak pressure profiles from cylinder with L/D = 1.0.[1]

For distances close to the charge ($Z < 11$ ft/lb$^{1/3}$) and as L/D decreases, the function becomes curved with a minimum pressure occurring at $\theta = 90^o$.[1] Alternatively, the opposite effect occurs as the L/D ratio becomes large and a maximum pressure is recorded at $\theta = 90^o$.

These results also demonstrate why traditional cube-root scaling cannot be used close to cylindrical charges.[21] As L/D increases, the pressures around the center of the cylinder ($\theta = 90^o$) become higher than at other angles. This phenomenon is noted in TIC-11268, which points out "the largest overpressure always occurred in the direction of the charge face with greatest presented surface area."

5.0 AIRBLAST LOADING OF STRUCTURES

For an internal blast, the majority of the energy coupled to a building from an airblast comes from the interaction of the shock waves within the structure. The pressure wave from an airblast creates a force on the internal area of the structure. This force is known as shock loading and is very brief (on the order of milliseconds) compared with other common types of loading (wind, seismic, etc.). A typical free-air shock is divided into three events. The time of arrival (TOA or t_a) marks the beginning of the shock with a discontinuity, or jump, in pressure and material properties. The positive pressure duration where the pressure rapidly decreases follows this jump. The final phase is the negative pressure phase when the low pressure formed from the outward expanding gasses causes a particle flow back towards the source of blast. A typical airblast pressure versus time profile is seen in Figure 19.

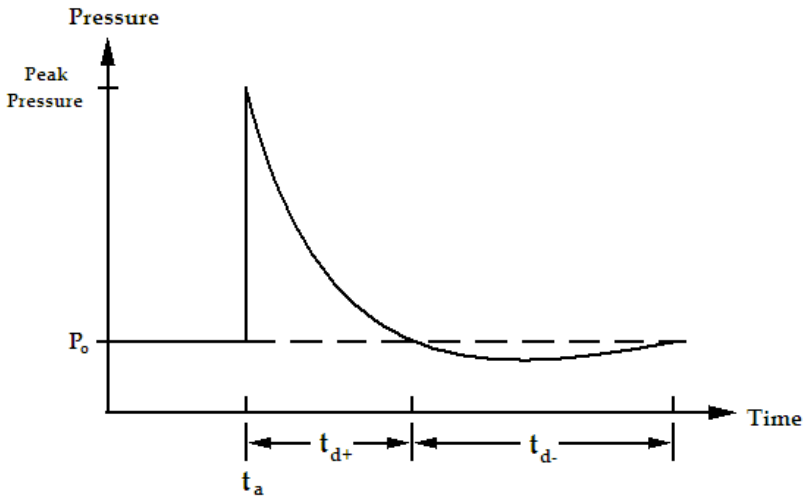

Figure 19: Typical pressure-time curve for a free-air shock.

The total loading from a blast wave is usually expressed as the impulse, or the integral of the pressure-time curve. The magnitude of the ambient atmospheric pressure, which is generally much less than the peak pressure, limits the negative pressures. This phase is usually ignored when calculating the force on a structure, and thus the impulse is only calculated for the positive pressures. Mathematically, the impulse is found from the following:

$$I = \int_{t_a}^{t_{d+}} P(t)\, dt = \Delta mv \qquad (5.1)$$

A unit analysis shows that impulse is equivalent to the time rate of change of momentum. This result comes by recalling that pressure is a force per unit area and force is equal to mass times acceleration. Thus, one can think of the impulse as the momentum imparted over time from the moving air particles.

5.1 Effect on Structures

The energy contained in a blast wave can be very destructive to objects that it encounters. This high energy is usually manifested as a pressure pulse (described above), which exerts a force over an area. Because of the rapid attenuation in pressure from the spherical divergence of a blast wave, the distance of the object from the charge center is a very important factor. Also important is the duration of the shock loading that contributed to the *impulse* delivered to the structure.

For simplicity, most air shocks can be mathematically treated as an equivalent triangular pulse.[14] This approach is generally based on the actual positive duration of the shock, but uses a linear decay approximation instead of the actual decay on the pulse. A triangular pulse forcing function on a spring-mass system can be mathematical evaluated

using the Duhamel integral to give the *response spectrum* of the system. This general solution allows for analysis of structural response of spring-mass systems by analyzing the maximum response ratio of the structure. This ratio is known as the dynamic magnification factor (DMF or Γ) and represents the ratio of the dynamic displacement to the equivalent static displacement. Figure 20 shows the response spectrum plot for a triangular forcing function.

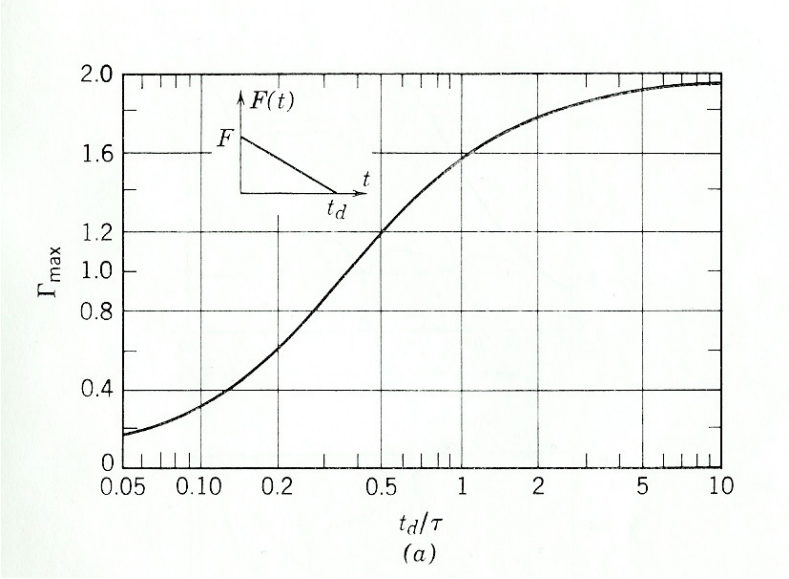

Figure 20: Dynamic magnification factor for a triangular impulse load on a single degree of freedom system.[22]

The ratio of the pulse duration to the natural period (t_d/τ) of the structure is very important for dynamic excitation. As the duration of the triangular forcing function (i.e., positive phase of the shock) increases, the DMF approaches a maximum value of two. The region between $0.05<t_d/\tau<1.0$ represents an increase of almost eight times in the DMF. In the testing of Building 340, the structures of interest were often not the entire bay, but a single wall. The explosive loading of a bay occurs so quickly that the walls will respond independently of each other according to their own natural frequencies. The natural frequencies of the concrete walls can be calculated assuming they are plates

clamped on all edges. Calculations Wilke performed give values of approximately 25 Hz for the ceiling (τ = 40 ms) and 40 Hz for the walls (τ =25 ms).[23] The positive phase of the initial shock pulse is typically 1–2 ms. Essentially, the blast will load the bay walls instantaneously with little chance for coupling with the structure's natural frequency. It is true that it takes a finite amount of time for the shock to propagate across the wall surface, which essentially lengthens the duration of the shock loading, but not enough to be of importance.

5.2 Effects of Airblast Confinement

We have already seen that a shock interaction with a surface generates a much higher reflected pressure than the incident wave because of the difference in shock impedances. When blast loading of structures is addressed in textbooks, typically the concern is for unconfined explosions that interact with building exteriors. Most of these books are concerned with the effects of nuclear weapons or conventional explosives that are detonated close to buildings by an accidental explosion or an intentional act. The sources for these texts are usually defense-related and often address the issue of dynamic loading on the faces and roofs of closed rectangular structures. For these unconfined blast interactions, the loading from a Mach stem is one of the greatest concerns.

However, the problem becomes different when the structure is being *internally loaded.* Because the explosion is occurring inside of the structure, the walls are loaded several times by the reflected shocks, and the pressures can build up from the detonation gasses unless they are relieved by venting. In Building 340, most of this venting came from the removal of the blow-out panels, but some venting occurred to the adjacent bay

and remaining building. The process of an internal blast loading is usually divided into the shock loading and quasi-static gas impulse phases.[1]

The shock loading discussed previously would be similar for a confined blast. In such a scenario, the structure would be initially loaded with the reflected pressures from the airblast. The pressure waves would be greatly attenuated by expansion and dispersion in the air, but will re-reflect off the walls and give additional impulse to the structure. For a centrally located detonation, using the first three reflected waves for the structural response calculations is suggested.[1] Each pressure peak is estimated to be half the magnitude of the previous. The shock velocity for these first three waves will be approximately constant, so the time between peaks should be equal.

Test data showed the decay in pressure between subsequent pressure peaks is much larger than the one-half decrease suggested. Therefore, only the first two peaks are significant, and the timing is much longer than estimated from assuming a uniform shock speed. Section 7.0 discusses this further.

6.0 GAS IMPULSE PHASE

After the first few shocks and reflections from a confined airblast, the unvented gas pressures throughout the room are usually assumed to reach a semi-uniform decaying level. This becomes more of a concern with increased confinement of the explosion. Additionally, the secondary reactions increase the temperature and pressure inside of the bay and contribute to the *gas impulse phase*.

A method of calculating the equivalent "quasi-static" pressures can be found in TIC-11268 and allows for the calculations of the gas impulse given the vent area and scaled parameters for the charge weight and room size. Using this method, predictions for the gas impulse were made based on the 25-lb test. The scaled wall thickness calculated for the 3-in. blow-out panel was found to be zero, implying that the panels would be removed quickly to allow venting. A scaled panel mass was found, and a vent area used was for the blow-out panel and the area leading to the adjacent bay. This calculation gave a gas impulse of $i_g = 2520$ psi-ms with a duration of $T_d = 19$ ms. This result refers only to the impulse resulting from the decay of quasi-static pressures. For a conservative comparison, the impulse from the abutting wall gauge, which represents higher reflected pressure values, was calculated over 30 ms and included the initial shock impulse. The JCAT-340 test data gave a positive impulse of 471 psi-ms, while the AUTODYN model calculated 400 psi-ms.

Other calculations using this method resulted in impulse predictions that were too high. A possible reason could be that the calculation method is partially based on a

computer code and not empirical data. Additionally, JCAT-340 test data showed that the quasi-static pressures were not usually seen because the pressures were quickly relieved through the vent area after the removal of the blow-out panels.

6.1 Contribution of the Secondary Reactions

Typical calculations for the blast loading of structures ignore the effects of secondary reactions in the expanding explosion product gas. However, very large fireballs can result from underoxidized explosives and may substantially damage a structure, especially if combustible materials are present. Overall, the fireball has a much smaller radius of influence than an airblast and is generally only encountered "close" to the charge. The complete combustion of the detonation products represents an increase in energy of 233% for TNT and 70% for PBX-9501.

The fireball from a high-explosive detonation occurs as the gaseous products expand into the surrounding air and combust with the atmospheric oxygen. The chemical reaction continues in the turbulent flow of the detonation products expansion. The exothermic combustion of the expanding reaction product gas releases large amounts of heat. This heat further sustains the process, but eventually the process will terminate because the reactions will either reach equilibrium or more likely become too mixed with the air to react. The later reason is a result of the lower limit of combustion for the particular secondary reaction.[9] This limit generally also controls when the combustion reaction will begin because the detonation products are pulled into air from a highly concentrated state. The ignition of the detonation products can occur from a direct flame source, a high-temperature region, or indirectly from high-pressure regions such as shock interactions.

Kuhl et al. suggest that the combustion process is controlled by convective mixing in a highly turbulent field.[24] They modeled the combustion of TNT detonation products using a "kinetic equation" for the process of the form:

$$x'(t;\lambda,n,T) = \frac{\lambda}{T}\frac{\left(1-t/T\right)^{n} e^{\zeta(t)}}{e^{\lambda/(n-1)}-1} \text{ where } \zeta(t) = \frac{\lambda\left[1-(1-t/T)^{n+1}\right]}{(n+1)} \quad (6\text{-}1)$$

The parameters λ, n, and T are fit to the empirical data and depend on factors such as confinement. Because of the many variations between the JCAT-340 tests, this type of equation is impractical.

6.1.1 Detonation Reactions and Product Hierarchy

Predictions of the energy released through the combustion process can be made with some assumptions and simplifications. Essentially, the problem is reduced to determining the amount of energy released and the time it takes to be released. A combustion process is much slower than a detonation and releases a significant amount of energy as heat and thermal radiation. The maximum energy from the secondary reactions can be calculated as the heat of afterburn (ΔH_{AB}), which is the difference between the heat of detonation and heat of combustion for the explosive. Two important equilibrium reactions encountered are shown below. The first is known as the water-gas equilibrium and is very important in the detonation reactions.

$$CO_2 + H_2 \rightleftarrows CO + H_2O \qquad \Delta H_r = 9.8 \text{ kcal/mole}$$

$$CO + O_2 \rightarrow CO_2 + \tfrac{1}{2}O_2 \qquad \Delta H_r = -67.6 \text{ kcal/mole}$$

The term ΔH_r is the heat of reaction calculated from the heats of formation for the compounds involved. CHEETAH calculated the products of detonation based on the

thermo-chemical equilibrium of the detonation reactions.[25] Figure 21 illustrates these products.

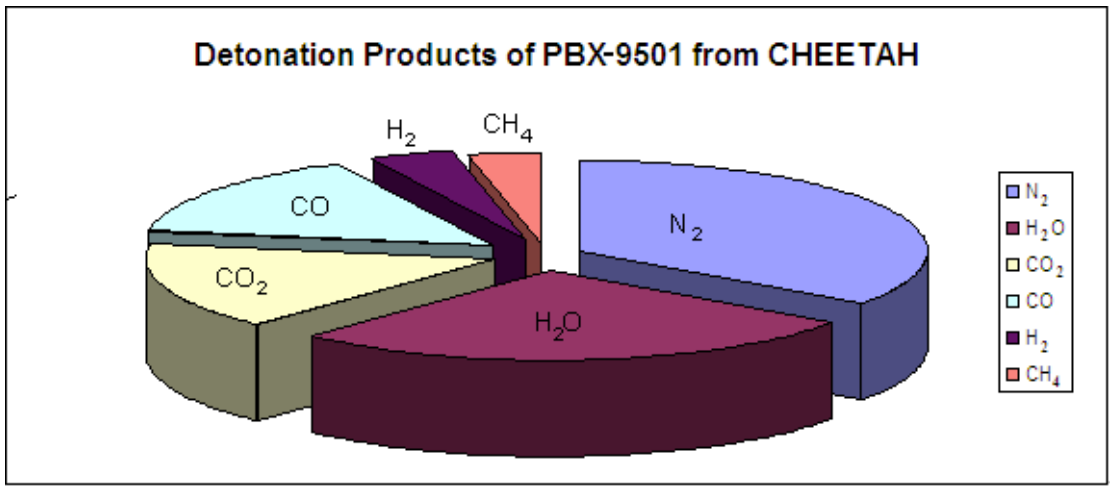

Figure 21: Detonation products of PBX-9501 calculated from chemical equilibrium.

As a comparison, the Kistiakowsky-Wilson rules provided a simple estimate of the detonation products of HMX (which makes up 95% of PBX-9501). One mole of HMX will yield four moles each of carbon monoxide, water, and nitrogen (33.3% of each).[8] These rules do not consider the lower fraction products that CHEETAH can calculate. The most common detonation products involved in the secondary reactions are solid carbon, carbon monoxide, and hydrogen. Because these products are formed almost instantaneously upon detonation, the real problem is modeling their combustion. Video data from explosion tests shows that the fireball starts almost immediately and expands outward falling further behind the shock front.

6.1.2 Effects of Confinement

Once again, the cylindrical charge geometry and confined nature of the explosions can complicate the process. For example, uncombusted material is more likely to ignite from the high pressures of reflected shocks off the confining surfaces. This result turns

out to be important for larger charge sizes in the JCAT-340 tests. Additionally, the confinement of an explosion can play a large role in the extent of the secondary reactions. For a large confined charge, the concentration of detonation products will be higher for a longer period. With little venting, the temperature and pressure of the event will remain elevated and drive the combustion process. On the other hand, the amount of oxygen available for the secondary reactions may be limited or insufficient for complete combustion.

6.1.3 PREDICTIONS FOR FIREBALL SIZE

Limited information is available on the duration and size of a fireball from the secondary reactions. Cooper presents a plot of peak overpressures versus scaled distance from an airblast that includes a scaled distance for a TNT fireball radius.[9] Because this scaled distance is a constant, it implies that the relationship between the charge size and fireball radius is approximately a cube-root function. Using this reference, the following relationship was derived.

$$D = 8.13 \times W^{1/3} \qquad (6\text{-}2)$$

The charge weight, W, has units of pounds, and D is the fireball diameter in feet. An additional estimate for the fireball diameter of an equivalent TNT charge was obtained from propellant explosions researched at Great Britain's Health and Safety Executive (HSE).[26]

$$D = 8.5 \times W^{0.341} \qquad (6\text{-}3)$$

Given these two empirical predictions, deriving a mathematical prediction for the fireball size based on knowledge of the secondary reactions was desirable. This prediction would

allow for the investigation of fireballs from additional underoxidized explosives (i.e., TNT vs. PBX-9501).

The first step was determining the amount of gas evolved by the detonation either from a hierarchy such as Kistiakowsky-Wilson or from CHEETAH. Then the amount of air needed for complete combustion can be calculated. The sum of these two represents the total amount of gas for the combustion process. Because this process will liberate energy (ΔH_{AB}), the temperature of the reaction will cause the volume of gas to expand according to the ideal gas law. The temperature of the reaction can be found by an adiabatic flame calculation similar to that presented in Cooper.[9] The product gasses gain heat given off by the secondary reactions such that

$$\Delta H_{AB}^{0}\, n_{HE} = n_{CG} \int_{T_0}^{T_a} C_p\, dT = n_{CG} \int_{T_0}^{T_a} \left(a + bT + cT\right)^2 dT \qquad (6\text{-}4)$$

It is assumed that the fireball combustion progresses in an unconfined state and will reach an end state of local atmospheric pressure. Because the ratio of moles of combustion gas per moles of HE $\left(n_{CG} \big/ n_{HE} \right)$ is a constant, the temperature calculation is independent of charge size. The temperature found from Equation (6-4) can be used with the ideal gas law assuming a spherical volume to find the theoretical diameter of the fireball. Solving for the diameter of the fireball, in feet, results in the following:

$$D = \left(\frac{6}{\pi} \frac{n_{CG} R T_a}{P} \right)^{1/3} \times \frac{10}{30.48} \qquad (6\text{-}5)$$

The n_{CG} term is the total amount of gas involved in the combustion process. Specifically, this value is found from the following:

$$n_{CG} = n_{HE}\left(\frac{n_{DG}}{n_{HE}} + \frac{n_{o_2 needed} / n_{HE}}{0.21}\right) \qquad (6\text{-}6)$$

This equation can be further simplified, but it is convenient to express the number of moles of detonation gas and oxygen needed as a ratio to the moles of high explosive. Appendix B provides details of this calculation for the explosive PBX-9501. If the theoretical fireball size predictions for TNT and PBX-9501 are expressed in the same format as Equations (6-2) and (6-3), the following equations are obtained:

$$\text{TNT: } D = 9.21 \times W^{1/3} \qquad (6\text{-}7a)$$

$$\text{PBX-9501: } D = 6.756 \times W^{1/3} \qquad (6\text{-}7b)$$

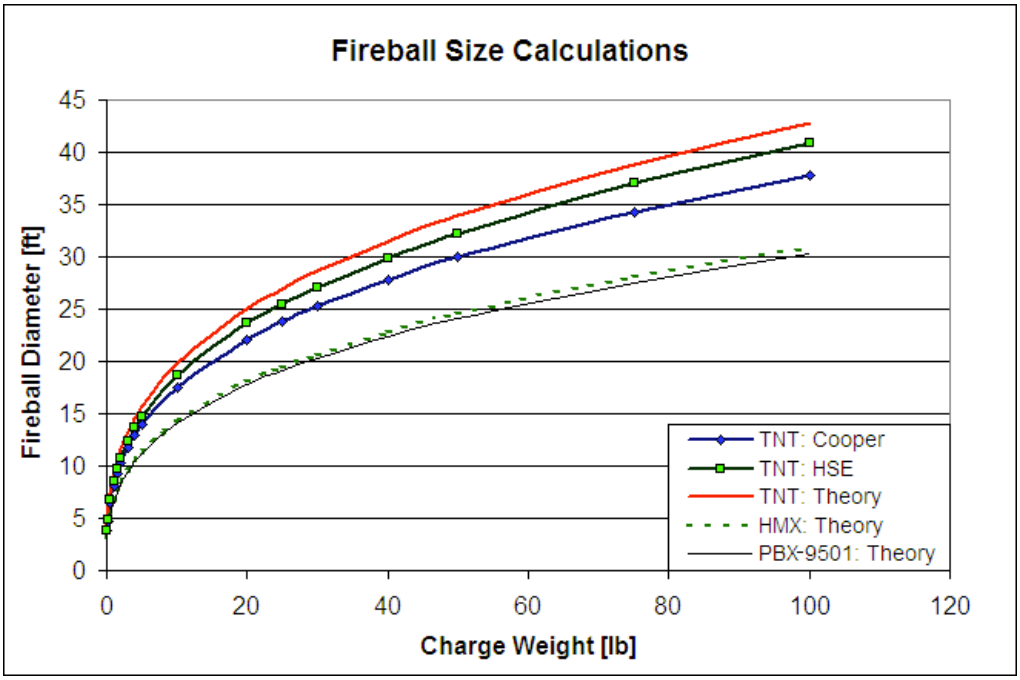

Figure 22: Empirical and theoretical predictions of fireball size.

Figure 22 presents the results from the comparison of fireball calculations. The fireball calculation for HMX offers a reasonable approximation for PBX-9501 as one might expect. The fireball predicted for PBX-9501 is considerably smaller than that of

TNT, a difference that is largely a consequence of the oxygen balance. The theoretical calculated fireball diameter for TNT is larger than the two empirical-based predictions. This result is expected because the actual combustion process is not likely to reach completion before the detonation products become too dispersed in the air. Some energy will be lost and not participate in the direct heating of the combustion gasses. This loss might include energy for thermal radiation, heating the structure, or convection into the surrounding air.

6.1.3 PREDICTIONS FOR FIREBALL DURATION

The time duration of the fireball is dependent on the kinetics for the combustion reactions, the charge size, and the extent of confinement. For the JCAT-340 charge size, the process will most likely occur over a few hundred milliseconds. Baker et al. proposed the following theoretical relationships for fireball growth and duration.[27]

$$D = aM^{0.333} \quad \text{and} \quad t = bM^{0.333} \qquad (6\text{-}8;\ 6\text{-}9)$$

The terms a and b are constants that depend on the particular explosive, and M is the charge mass. This is consistent with the prediction of Equation (6-5) because all of the parameters for a particular explosive can be reduced to a single constant and become a cubic-root function of charge weight alone. These constants (a and b) are presented for several propellants in the HSE reference with some deviation from the cubic-root dependence. The fireball size predictions include two functions for TNT fireballs, but constants for time duration do not include values for TNT. However, the constants given for the fireball diameter of "Munitions" are very similar to the TNT constants. It was assumed that the time duration based on this material could be used for TNT predictions, which results in the following formula for TNT fireball duration:

$$t = 0.20M^{0.35} \quad (6\text{-}10)$$

The HSE Web site provided another source of information (referred to as HSE2 in Figure 23 to avoid confusion) for the time duration of explosions in chemical warehouses.[28] Based on the form given in Equation (6-8), the equation given for fireballs similar to those from hydrocarbon liquids can be reduced to the following:

$$t = 0.0237D \quad (6\text{-}11)$$

The referenced equation has been changed to keep symbols and units consistent. This equation can easily predict fireball durations of TNT or PBX-9501 because the calculation is directly related to the fireball diameter.

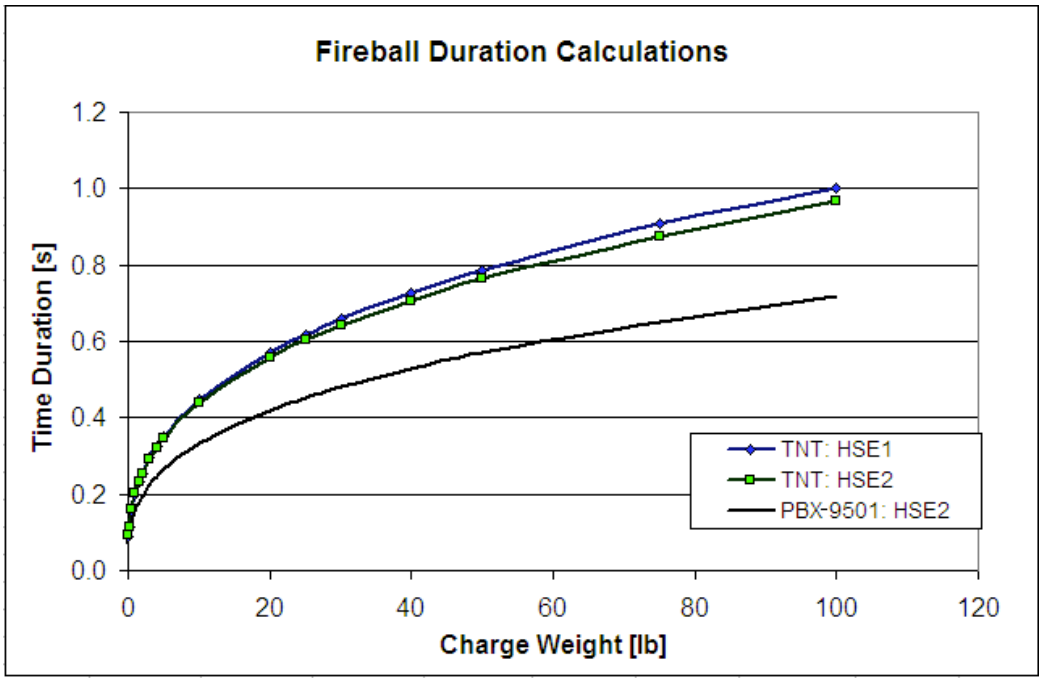

Figure 23: Predictions for fireball duration of TNT and PBX-9501.

The fireball duration for PBX-9501 is shorter than that of TNT because of the difference in oxygen balance. These durations are orders of magnitude larger than the positive pulse duration for a shock wave. A fireball from a confined explosion might

possibly result in a long duration impulse that would be able to couple with the structure's natural period and cause the structure to respond in phase with the loading.

6.1.4 Separation of Fireball from Shock Boundary

High-speed video for the detonation of high explosives shows that initially the fireball growth occurs directly behind the shock wave being formed. However, after some expansion of the gasses, the secondary reactions separate from the shock boundary. This separation becomes more pronounced because the fireball will reach a maximum size, whereas the shock will continue to propagate for a much larger distance. This effect is not well documented for chemical explosions, but the study of nuclear explosions has resulted in some understanding in the phenomena involved.

At temperatures below ~5000 K, the luminous phenomenon occurring from the secondary reactions is largely attributed to reactions involving nitrogen dioxide.[29] However, this mechanism for absorption and emission for visible light does not occur below 2000 K. At temperatures below this critical value, "a luminous disk with a radius smaller than the radius of the shock front becomes visible."[29] At this point, the fireball separates from the shock boundary. After this point, the fireball radius increases until the pressure drops to approximately atmospheric as shown in Figure 24.

The reactions that occur in the secondary combustion process for high explosives will not be the same as those in a nuclear explosion. The reactions occurring with the latter occur with the air molecules already present, not with gasses introduced from the explosion. The formation of nitrogen dioxide does occur, but in small quantities.

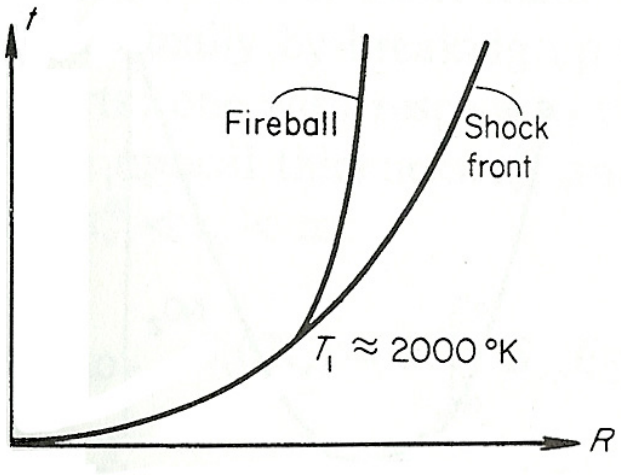

Figure 24: Separation of shock front from fireball boundary.[28]

A plot of positive phase duration with scaled distance, such as presented in Cooper, can provide additional insight into the process. At a small scaled distance from the charge, no negative pulse is measured from an airblast. Initially, all detonation product gasses move away from the initiation point, but at some time later the particles will slow or even reverse direction until equilibrium is obtained with atmospheric pressure, resulting in two extremes. Very close to an HE charge, there is no negative pulse, but, by the time the pressure wave has reached acoustic levels (very far away), the positive and negative phases are approximately equal.

6.2 Effects of Thermal Radiation on Measurements

The thermal radiation from the secondary effects can have undesired effects on piezoelectric pressure gauges. Because the quartz used in the gauge is a semiconductor material, exposure to electromagnetic radiation (i.e., light) can produce a thermoelectric response and cause measurement error. Radiant heat from the fireball or heat from convection of hot gasses flowing around the gauge can cause this error.[30] The quartz crystals used in the piezoelectric gauges are not especially sensitive to thermal shock, but

an increase in temperature can cause case expansion, which lessens the preload force on the crystals. This change in turn will cause a negative shift in the gauge output.[30] The most common way to prevent thermal effects on the gauge is to cover the exposed sensor with an opaque material, such as silicone grease, RTV silicone rubber, vinyl electrical tape, or ceramic coatings. The JCAT-340 tests used a combination of aluminized Mylar and vacuum grease.[4]

7.0 ANALYSIS OF JCAT-340 TEST DATA

The theories and ideas presented in the preceding sections were applied to the JCAT-340 test data to develop an understanding of the phenomena that occurred. Variations in the charge placement and bay geometries of the shots made it difficult for a direct comparison between the test data. Because the tests with blow-out panels were at a lower (1-m) charge height, a large ground shock formed that was very influential on the airblast behavior. All of the tests in this analysis used cylindrical charges of PBX-9501 that were oriented with the axis perpendicular to the ground and end-initiated at the top surface. The charges were located in the center of the bay with respect to the walls. Specifically, this location was 13.5 ft from the back wall and 10 ft or 12 ft from the abutting and adjacent walls depending on bay width (see Table 5).

Charge Weight [lb]	Charge Height [m]	Bay Width [ft]	Charge Length [in]	Charge Diameter [in]	L/D
5	2	24	5.331	4.25	1.25
25	1	20	7.25	8	0.91
50	2	20	6	12	0.50
75	1	24	9.63	12	0.80
100	2	24	12	12	1.00

Table 5: Summary of tests analyzed.

The pressure history can be divided into the initial pressure pulses and late-time behavior. The term “late-time” refers to the period after the first few shock interactions (generally after ~20 ms) when any effects from secondary reactions would occur.

Three-dimensional AUTODYN models modeled each test with the explosive detonation calculation remapped from a separate 2-D model. These models used cubic cells (elements), with each side having a length of 1/3 ft or 10.16 cm, and had an average of 800,000 cells each. The tests used the actual charge dimensions, atmospheric conditions, and building dimensions. The JCAT-340 test data and AUTODYN models used only the reflected pressure gauges in the test bay as shown in Figure 25.

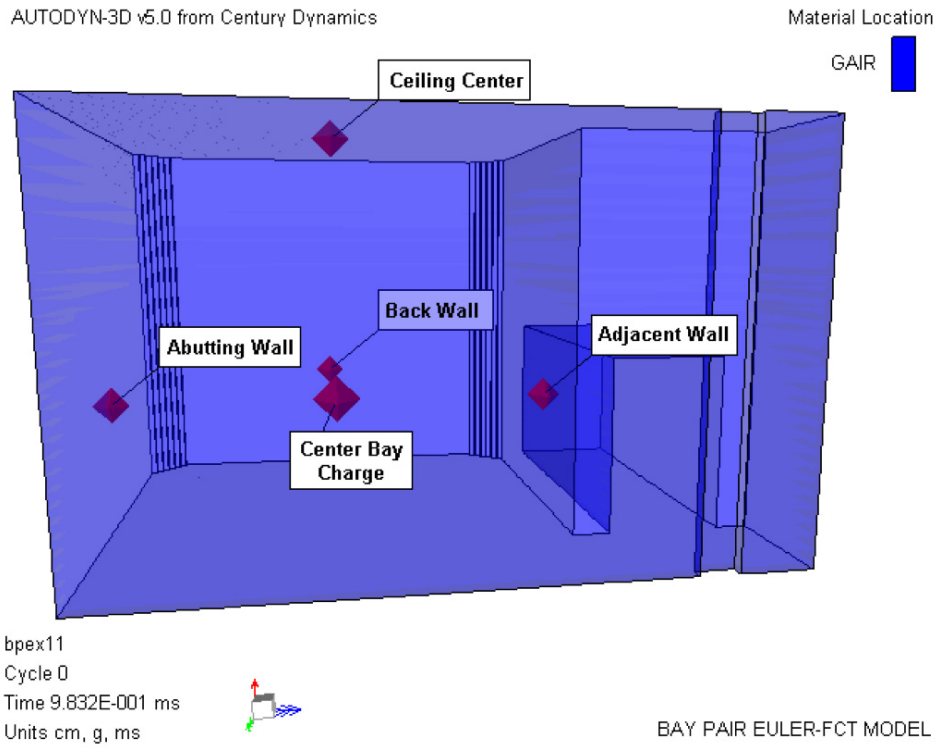

Figure 25: AUTODYN 3-D model set-up with gauge locations.

7.1 Comparison of AUTODYN Models to Test Data

Pressure readings on adjacent and abutting walls were similar because of the symmetry of the charge placement in the bay. Figure 26 shows this placement for the 25-lb shot. Only one data set is shown for the AUTODYN 3-D model data because the abutting and adjacent wall gauges were essentially identical up to 15 ms. However,

differences arose after a few reflections inside the bay because of the asymmetries in the structure. For example, the adjacent wall had an opening to the rest of the building and was consequently shorter than the abutting wall. The blow-out panels were "removed" from the model calculation at 12 ms by defining a material flow-out boundary condition at the location of the panels. This removal time corresponds to the time it took for the initial shock wave to travel up the panels, reflect off the ceiling, and travel about one quarter of the way down again. Recall that the artificial viscosity methods cause the predicted pressures to have lower peak values and occur later in time (see Section 4.1).

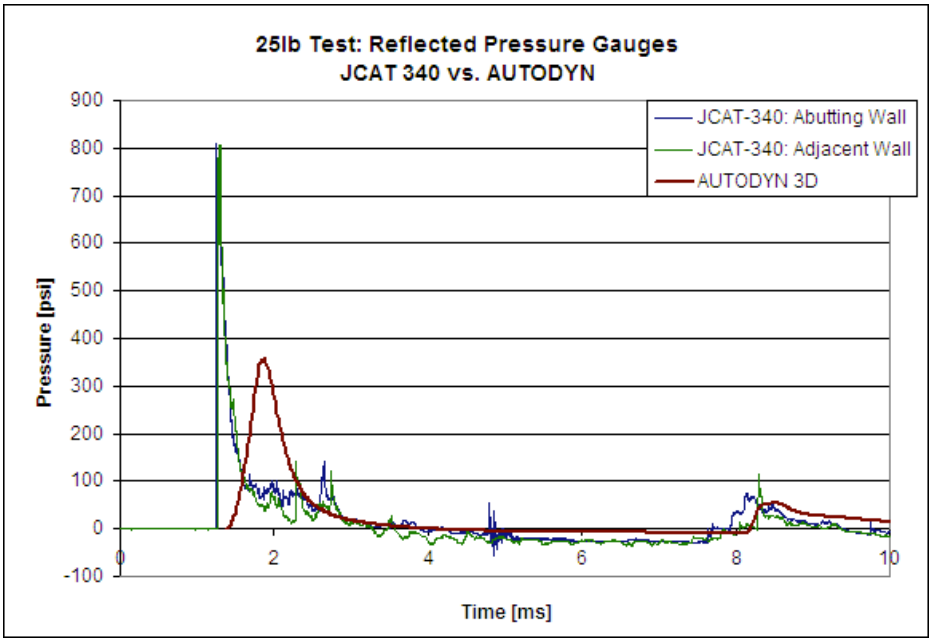

Figure 26: Experimental and predicted pressure data comparison for the 25-lb test.

Figure 27 shows the comparison between actual and predicted pressures for the back wall and ceiling center gauge locations. These gauges were located farther away from the charge, so the time scale for these gauges has been extended to 15 ms.

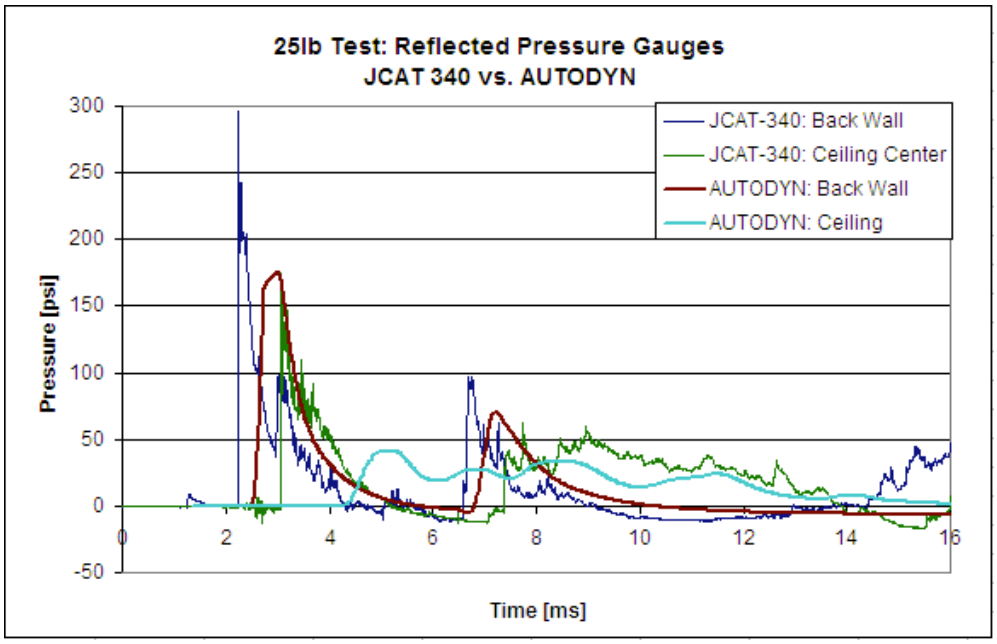

Figure 27: Back wall and ceiling pressure data comparison for the 25-lb test.

One benefit of using a finite element method for modeling an airblast is the ability to predict the entire pressure-time history. Although the peak pressures predicted by AUTODYN 3-D were lower than the actual test data, Table 6 shows that the impulse calculated from the positive pressures matches well between the two. For structural calculations, this parameter is more important than simply knowing the peak pressure because it represents the amount of energy that will be delivered to the structure.

Positive Impulse at 7 ms [psi-ms]				
	Abutting Wall	Back Wall	Adjacent Wall	Ceiling Center
JCAT-340	222	165	182	99
AUTODYN 3-D	209	165	209	72
Positive Impulse at 20 ms [psi-ms]				
JCAT-340	278	352	200	293
AUTODYN 3-D	313	312	309	221

Table 6: Comparison of positive impulse for gauges in 25-lb test.

Several smaller peaks occur after the initial shock front in both the AUTODYN models and the actual JCAT-340 data for gauges located in the test bay. These peaks are

from the multiple shock reflections between the bay walls that arose because of the confinement of the airblast. These reflections occurred as the shock reflected off the ceiling and walls to form reflected pressure waves that traveled down along the walls and were recorded at the gauge locations. For example, a secondary peak would occur at the back wall gauge because of the reflected shock off the adjacent and abutting walls. The shock reflection from the ceiling can also contribute to this. Figure 28 illustrates a numerical snapshot from the 100-lb AUTODYN 3-D model.

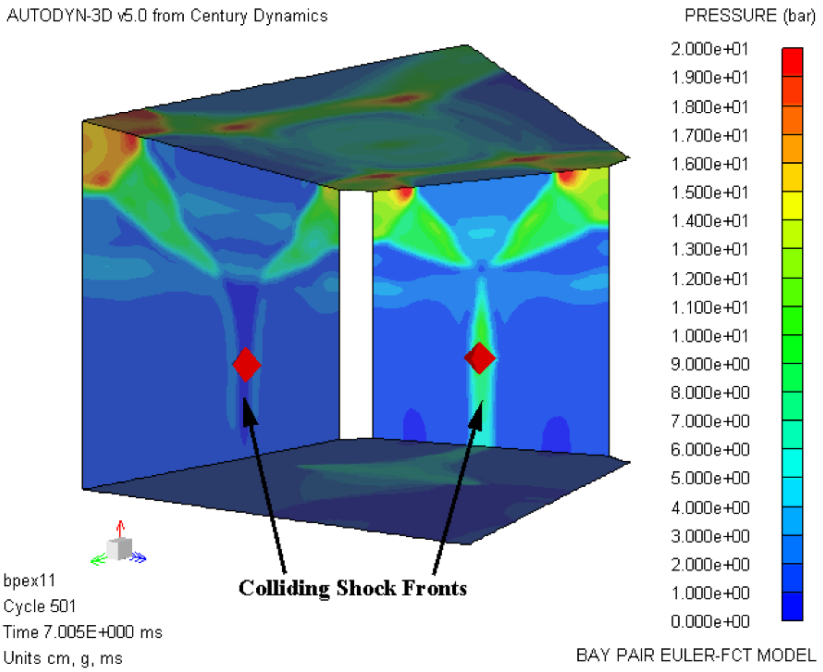

Figure 28: Secondary peak pressures caused by reflecting shocks from 100-lb charge.

7.2 Effects of Charge Height and Presence of Blow-Out Panels

As discussed in Section 2.1, the blow-out panels were still in place for the first few tests in Building 340. The blow-out panel required a finite amount of time to accelerate because of its inertia, and consequently a few shocks are reflected off the panel before the gasses can be vented. This reaction influenced the propagation of shocks into

the rest of the building and caused the pressures in the adjacent bay and hallway to be higher than if the panels were initially removed.

The one-meter charge height in the 25-lb and 75-lb tests resulted in a large amount of shock reflection off the floor. This reflection caused differences in the shock wave profiles and airblast phenomenon between the two charge heights. Figure 29 shows the pressure-time profile for both of the one-meter charges and a 50-lb charge (2-m charge height) for comparison. The small pressure pulse immediately following the initial shock wave in the 50-lb data resulted from the shock reflected off the floor.

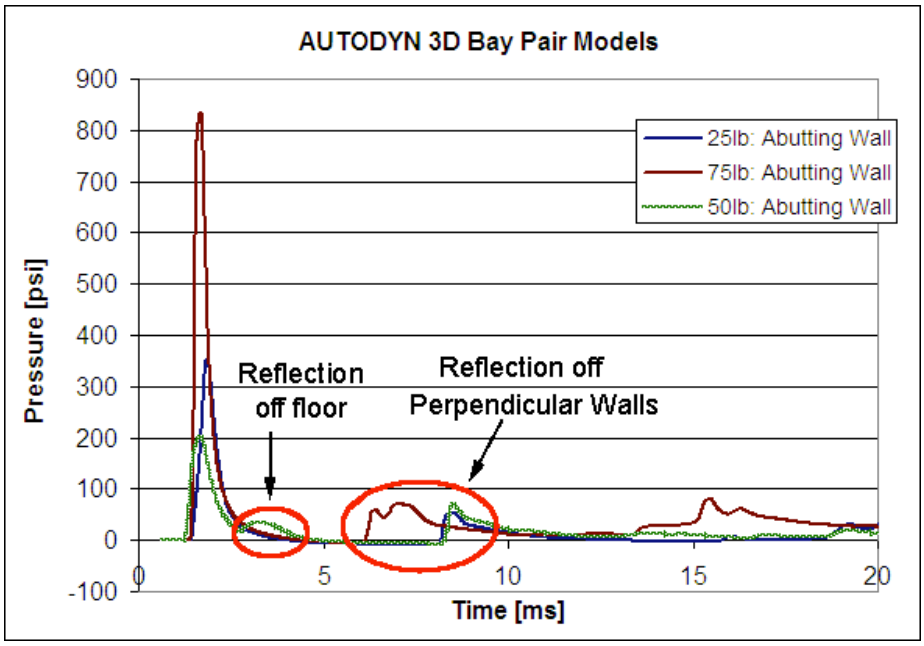

Figure 29: AUTODYN 3-D model comparison for initial shock.

For the one-meter charge height, AUTODYN models showed that the reflected floor shock overtakes the original shock by the time it reaches the wall gauges, and only a single pressure pulse was recorded. Consequently, the peak pressure predicted by AUTODYN from the 25-lb shot was higher than the 50-lb shot even though both tests occurred in 24-ft-wide bays. Figure 30 shows the remap file for the 75-lb AUTODYN

model and demonstrates the Mach stem that develops along the floor. The locations of the reflecting pressure gauges have been marked and appear to be in a direct line with the locus of Mach stem triple points. The JCAT-340 test data is consistent with the AUTODYN-predicted behavior in that the wall gauge peak pressures from the 25-lb and 75-lb tests were larger than the 5-lb and 50-lb tests respectively.

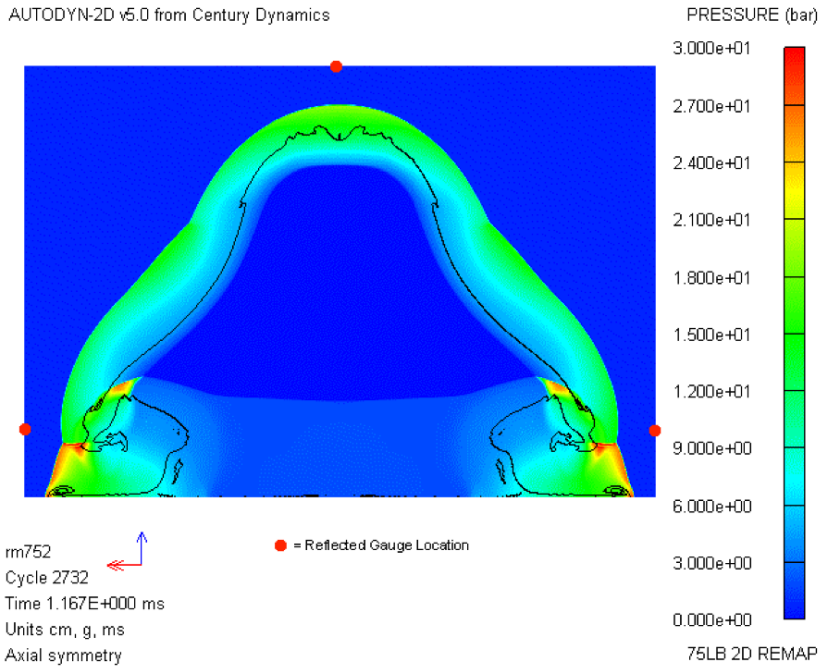

Figure 30: Airblast showing Mach stem formation for the 75-lb AUTODYN model.

7.3 Late-Time Impulse from Secondary Reactions

Test data analysis to this point has been for the pressure versus time history for only the first few initial pulses. For tests with charge sizes greater than 5 lb, a large impulse appeared later in time and can be attributed to the secondary reactions. Because the AUTODYN models use the JWL and ideal gas equations of state to calculate the pressures, they cannot provide any predictions for the reactive flow behavior in the secondary combustion reactions.

Figure 31 shows the late-time impulse associated with the secondary reactions for the 25-lb test. The adjacent wall gauge should be very similar to the abutting gauge, but it started to drift downwards after about 50 ms to record unrealistic pressures below atmospheric. This impulse lasted from approximately 25 ms to 300 ms and had a value of about 15,800 psi-ms at the abutting wall gauge, whereas the ceiling recorded 3,200 psi-ms. This reading represents a huge increase in impulse when compared with the impulse from the first few reflected shocks reported in Table 6.

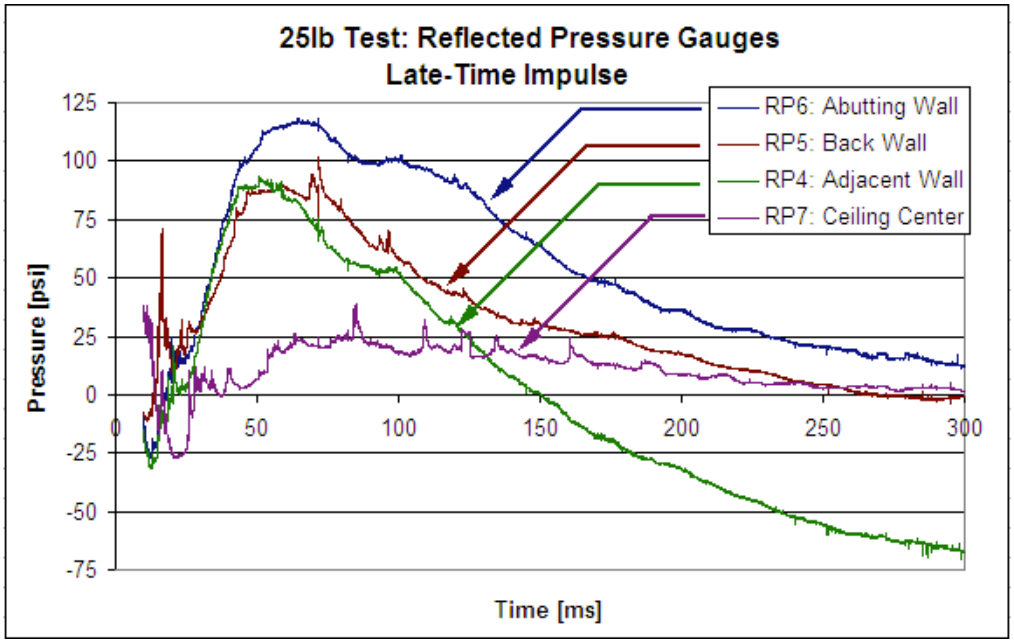

Figure 31: Pressures up to 300 ms for the 25-lb test.

Using the prediction method from Section 6.1.3, a spherical fireball for 5 lb of PBX-9501 would have a diameter of approximately 11 ft. Because this shot was carried out in a 24 ft bay, there was a good chance that the fireball would not touch the walls. Digital video data from this test (Figure 32) revealed that this prediction is correct. However, the actual fireball was toroidal in shape with a diameter of approximately 20 ft.

Figure 32: Test video from 5-lb shot showing fireball size.

Figure 32 shows a column of dark detonation products being projected towards the ceiling above the luminescent fireball. Earlier time video data showed the fireball propagating from the bottom center of the expanding gasses. The shock reflected off the floor seemed to contribute to the fireball initiation and to drive the combustion process upwards. As expected, and confirmed by the test videos, the shock traveled immediately ahead of the uncombusted detonation products. The fireball shape suggests that the preceding shock front had roughly the shape AUTODYN predicted (see Figure 30). The fireball combustion shown in Figure 32 has essentially completed by the next video frame (~15 ms later).

The 5-lb JCAT-340 test data shown in Figure 33 exhibits a slight rise in pressure for the wall gauges between 50 ms and 150 ms. This rise occurred because of the secondary reactions, but the fireball was not large enough to cause a substantial increase

in pressure as seen in the 25-lb data (Figure 31). Because the pressures at this point were below atmospheric pressure, the positive impulse did not increase.

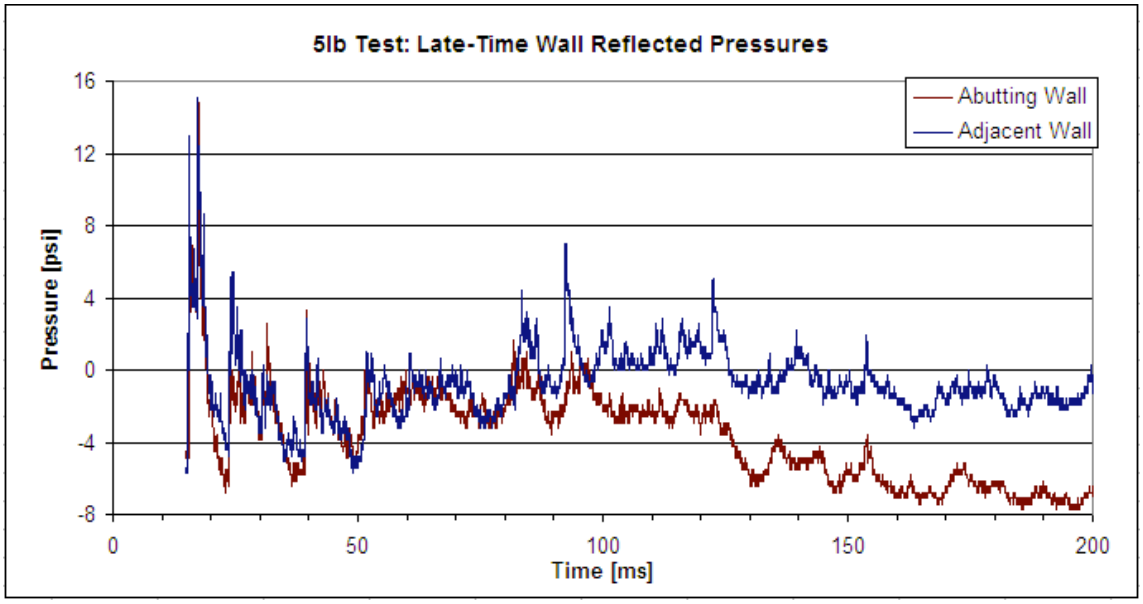

Figure 33: Pressures from 15 ms to 200 ms for the 5-lb shot.

7.4 Summary of Results

The remainder of Section 7.0 presents an overview of the peak pressure predictions and the secondary effects. The data is organized by increasing charge size.

7.4.1 PEAK PRESSURES AND INITIAL SHOCK BEHAVIOR

The values for peak pressure have been compiled from the JCAT-340 test data, pre-test predictions, post-test AUTODYN models, and BlastX predictions. The pre-test predictions are based on a correlation between early AUTODYN models and reflected pressure predictions from the DDESB-BEC. Although these early models used the correct charge size and atmospheric conditions, they all assumed a charge geometry with L/D = 1.0. Additionally, the reflected pressures from DDESB-BEC were for a hemispherical charge of TNT with the charge weight adjusted by an explosive

equivalency factor. The post-test AUTODYN data is from 3-D models that were corrected to match the tests' charge geometry and gauge locations. These models should provide a direct comparison to the test. The DRI data is based on incident peak pressures calculated for cylindrical charges [Equations (4-5) and (4-6)] then multiplied by a reflection factor [Equation (3-8)] based on a spherical shock front. The DRI data in bold print is within the range for accuracy of the curve-fit equations suggested in TIC-11268 (i.e., 2–100 psi for incident pressure). Finally, the BlastX data is for cylindrical charges of C-4 with L/D = 1.0. Because the TNT equivalency factor for C-4 is exactly the same as PBX-9501, this data should provide a close comparison.[1] Tables 7–10 below present the data grouped by each test.

Pressure Gauge Location	JCAT-340 Actual	Pre-Test Prediction	Post-Test AUTODYN	Actual/ Model	DRI w/ C_r	BlastX
Abutting Wall	58.4	85	26.0	2.2	**74.9**	34.3
Back Wall	36.3	67	24.6	1.5	**50.2**	24.5
Adjacent Wall	57.0	85	26.0	2.2	**74.9**	34.3
Ceiling Center	41.7	49	18.2	2.3	**48.4**	30.6

Table 7: Comparison of peak pressures for the 5-lb tests.

Pressure Gauge Location	JCAT-340 Actual	Pre-Test Prediction	Post-Test AUTODYN	Actual/ Model	DRI w/ C_r	BlastX
Abutting Wall	798	498	355	2.3	939	507
Back Wall	293	357	175	1.7	**295**	235
Adjacent Wall	805	469	355	2.3	939	507
Ceiling Center	175	100	41	4.3	**113**	299

Table 8: Comparison of peak pressures for the 25-lb tests.

Pressure Gauge Location	JCAT-340 Actual	Pre-Test Prediction	Post-Test AUTODYN	Actual/ Model	DRI w/ C_r	BlastX
Abutting Wall	638	1284	201	3.2	810	1157
Back Wall	370	462	130	2.8	**326**	403
Adjacent Wall	781	1201	201	3.9	810	1157
Ceiling Center	1125	360	321	3.5	**306**	1682

Table 9: Comparison of peak pressures for 50-lb tests.

Pressure Gauge Location	JCAT 340 Actual	Pre-Test Prediction	Post-Test AUTODYN	Actual/ Model	DRI w/ C_r	BlastX
Abutting Wall	1325	947	836	1.6	1569	1228
Back Wall	1441	1216	626	2.3	1020	863
Adjacent Wall	869	940	836	1.0	1569	1228
Ceiling Center	789	361	272	2.9	**354**	1571

Table 10: Comparison of peak pressures for the 75-lb tests.

Calculations using the DRI data, with the reflection coefficient, and the BlastX models appear to give the most accurate peak pressure predictions for most of the tests. However, these methods fail to consider the strong ground shock that occurred with a one-meter charge height. The ceiling center gauges were consistently much higher than AUTODYN predictions as illustrated in the actual-to-model column (peak pressure ratio) in Tables 7 through 10. This higher reading could result from small fragments that are propelled upwards from the detonation and are also influenced by the secondary reactions.

Data from the JCAT-340 tests showed that the most ideal shock wave pulses were recorded for the smaller charges (5-lb, 25-lb), whereas the data became increasingly chaotic for larger charges. Several factors can cause inaccuracies or anomalies among the data. Although the bays were cleaned and swept of any loose materials before the shot, the blast inevitably caused fragments to form from a number of sources such as the wooden test stand the HE charge was placed on. The debris and fragments could hit a gauge and cause spikes in the recorded pressure or complete gauge failure. Many of the cables and connections were laid on the floor for the test and could have been disrupted by the ground shock formed. As discussed before, the fireball could also have an effect on the gauge sensors—either from thermal radiation or the pressures and temperatures

generated during the combustion. All of these effects would become more apparent as charge size increases.

7.4.2 EFFECTS OF SECONDARY REACTIONS

The behavior of the secondary effects in the JCAT-340 tests differed greatly from the predicted behavior discussed in Section 6.1 because of the confinement provided by the bay walls and ceiling. For charge sizes larger than 50 lb, the fireball was *pushed* out by the expanding gasses so that a large amount of the combustion process occurred entirely outside of the bay (Figure 34).

Figure 34: Fireball being pushed out of the bay from a large charge size.

Table 11 presents predictions of the fireball duration for the JCAT-340 tests made using several methods. Because the method developed in Section 6.1 is for unconfined explosions, it results in erroneously large values. Alternatively, predictions can be made from the video data by knowing the frame rate of the camera and counting the number of frames until the combustion is complete. This method used the video data from both the HyCam II camera (high frame rate) and the digital camera (30 fps). Obtaining an

accurate prediction using this method was difficult because some of the tests had blow-out panels in place initially or because the camera was not in the direct line of sight of the fireball. The final predictive method consists of analyzing the pressure data recorded inside the bay and determining the fireball duration from the length of the late-time impulse.

Charge Weight [lb]	Theoretical Size [ft]	Duration [s]	Canon XL1S (Digital) [s]	HyCam II [s]	JCAT-340 Data [s]
5	11.18	0.264	0.050	N/A	0.100
25	19.12	0.452	N/A	0.103	0.225
50	24.09	0.570	N/A	0.085	0.230
75	27.57	0.652	0.400	0.267	0.260
100	30.35	0.718	0.172	0.140	0.270

Table 11: Predictions of fireball duration for JCAT-340 tests.

The most consistent predictions seem to come from the reflected pressure test data. However, this data only accounts for the fireball *inside* of the bay. Interestingly, the duration calculated by this method shows little variation between the 25-lb test and the 100-lb test. The bay size can only accommodate a certain amount of combustion before the excess gasses are pushed outside. Thus, the bay size limits the amount of gasses available for combustion that could affect the structure, and that amount remains a constant after a critical charge size. The combustion rate of the product gasses should remain relatively constant with charge size, which explains the consistency in fireball durations predicted from the reflected pressure gauge data.

8.0 ADDITIONAL COMMENTS ABOUT JCAT-340 TESTS

8.1 Cylindrical vs. Spherical Charge Geometry Effects

Models were run to investigate the difference in impulse delivered to a Building 340 bay from a cylindrical charge versus a spherical charge. For these models, a 100-lb charge was modeled at two meters above the floor and centered in a 24-ft-wide bay. The geometry of the explosive was a cylinder with L/D = 1.0 (consistent with the JCAT-340 test) and an equivalent weight spherical charge. Gauge points set up approximately every three feet formed arrays of targets in the ceiling and adjacent, abutting, and back walls. The pressure-time data from the AUTODYN gauge points was integrated to get impulse values out to 50 ms and then plotted in MatLab. Figure 35 shows a 2-D contour plot of the impulse magnitude along the internal bay surfaces.

After approximately 30 ms, the walls have experienced the majority of the airblast impulse. The impulse that occurs from 40–50 ms is typically less than 5% of the entire impulse out to 50 ms. Following this reasoning, impulse after 50 ms was neglected.

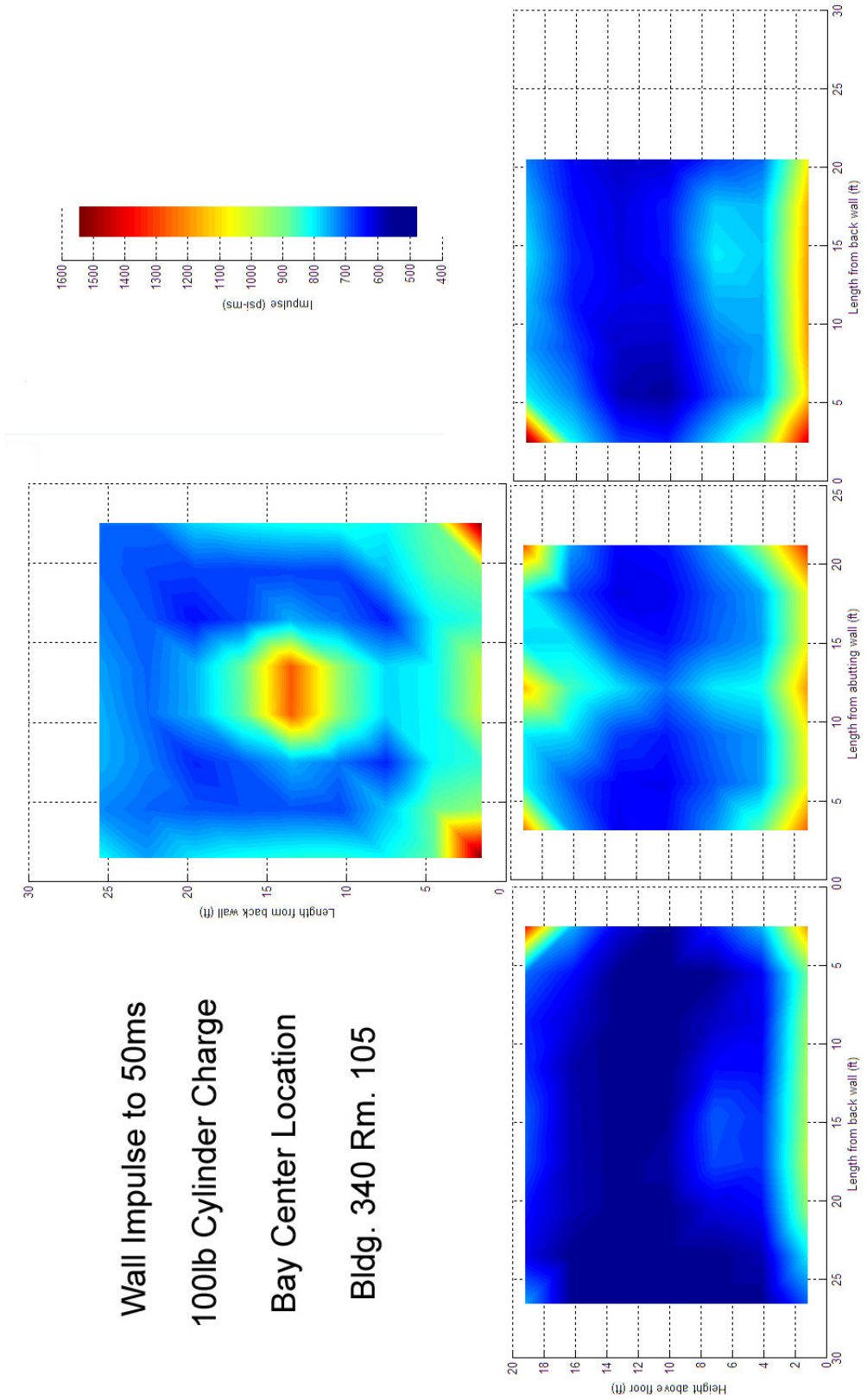

Figure 35: Impulse distribution contours on bay walls from a cylindrical charge with L/D = 1.0.

The same procedure repeated for an equivalent weight spherical charge determined mathematically the difference between the gauge point arrays. Figure 36 displays the most dramatic difference, which took place on the ceiling.

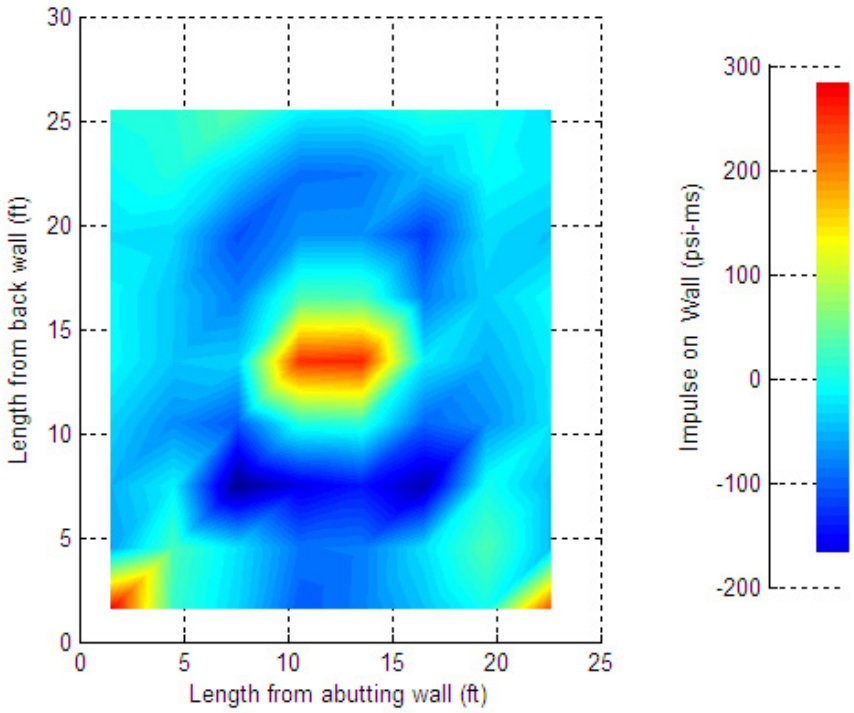

Figure 36: Difference between charge geometries for the ceiling.

Interestingly, the average impulse was about 3–5% higher for the spherical charge, but the cylindrical charge had regions of higher impulse. The highest impulse occurred directly above the cylinder and covered a circular area on the ceiling (the floor impulse was not analyzed). The walls had a slightly higher impulse region in the horizontal plane of the cylindrical charge. Regardless of the charge geometry, the room corners always had large impulses that resulted from the shock reflections.

8.2 Explosive Charge Density Effects

The possibility exists that explosive charges used for JCAT-340 shots would not use the density obtained from pressing ($\rho = 1.833$). This scenario would arise if loose prills of PBX-9501 were transferred into a container and packed to a uniform density. This analysis assumes the packing density achieved from this method would be approximately 1.0 g/cm^3. Because the density of a high explosive affects the detonation velocity, C-J pressure, and reaction kinetics, the detonation process for this test would vary from those using a higher-density explosive. The detonation velocity for the lower-density explosive can be predicted by the method given in Cooper:[9]

$$D = D' - 3(\rho_{TMD} - \rho_0) \tag{8-1}$$

The detonation velocity and density at the theoretical maximum density (TMD), D' and ρ_{TMD} respectively, could not be found for PBX-9501 in the available references.[12] However, Urizer's formula for mixtures can be extended for predictions of both by using values for the components at TMD.[9]

$$D_{mix} = \sum D_i V_i \tag{8-2}$$

This calculation gives values of $D_{mix} = D' = 8.99$ km/s and $\rho_{mix} = \rho_{TMD} = 1.87$ g/cm^3 at TMD. However, the literature value for PBX-9501 is $\rho_{TMD} = 1.855$ g/cm^3, so this calculation method may have some error.[12] The detonation velocity of PBX-9501 at the nominal density is 8.780 km/s, so using Equation (8-1) gives a new detonation velocity of D = 6.382 km/s. The C-J pressure can now be predicted from the formula:

$$P_{CJ} = \frac{\rho D^2}{4} \tag{8-3}$$

This method predicts a C-J pressure of 10 GPa. This value seems reasonable because CHEETAH calculations give values of P_{CJ} = 36 GPa for the PBX-9501 at its pressed density and P_{CJ} = 9.5 GPa for a density of one.

For explosives loaded at lower densities, the reaction products and chemical equilibrium shift to favor the formation of carbon monoxide.[9] Empirical data suggests that the ratio of CO to CO_2 is between two and three for an explosive with $\rho \approx 1.0$ g/cm^3. This result is quite significant compared with PBX-9501 at a nominal density of 1.84, which has ratios of zero and one using the Kistiakowsky-Wilson hierarchy and CHEETAH-predicted detonation hierarchy respectively. The videos confirm the difference in detonation product formation for explosive shots at a density of 1.0 g/cm^3, which show a large amount of smoke from partially burned detonation products.

CHEETAH has the capability of fitting JWL parameters to the detonation process for a specific energetic material composition and density. This capability was used to generate a set of JWL parameters for PBX-9501 at ρ =1.0 for use in AUTODYN models. An adiabatic tail fit method was chosen because the results were in best agreement to literature JWL parameters for the explosive at nominal density. However, a comparison of the pressures at gauge locations along the walls shows very little difference in the peak pressure and shock wave histories using the two different explosive loading densities. The large variation in detonation velocities for the explosives at the two densities results in only a trivial difference in the time duration (i.e., microseconds) for the detonation process. The energy per unit mass of the explosive will be the same regardless of the loading density. As a result, the same amount of energy is released in relatively the same amount of time so that the formation of an airblast is essentially identical. Consequently,

the change in loading density will most likely have a greater effect on the behavior of the chemical equilibrium and secondary reactions than the shock loading of the structure.

A rate stick model (Figure 37) verified the detonation velocity of the new defined explosive and checked the ability of AUTODYN to transmit detonation between two explosive materials by shock initiation. The rate stick was 200 cm long by 100 cm in diameter and composed of PBX-9501 at ρ =1.833 g/cm^3 (right) and ρ =1.0 g/cm^3 (left).

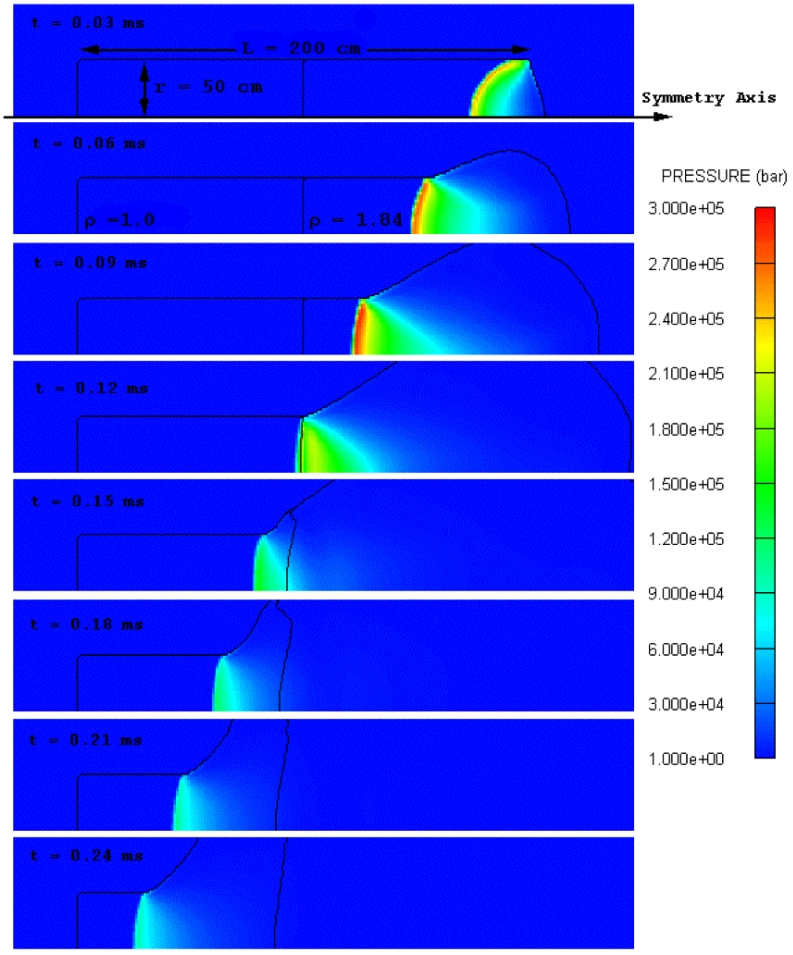

Figure 37: Rate stick model for the study of shock transmission between explosives and density effects for PBX-9501.

9.0 CONCLUSIONS

The JCAT-340 test series provided an excellent opportunity for analysis of current methods for predicting the behavior of cylindrical charges and the effect of secondary reactions occurring in confined structures. Several conclusions may be made based on the work presented in this thesis.

The pressure profiles that occur close to a cylindrical explosive charge are strongly dependent on the length-to-diameter ratio of the charge. At large distances from the charge, the eccentricities in the profile become negligible and the free-field airblast becomes increasingly spherical. For simple scenarios or determining single parameters such as peak pressures, finite-element codes (e.g., AUTODYN) may not be as accurate as more straightforward empirical-based methods. This result is in part due to the artificial viscosity and computational methods a finite element program employs that limit the accuracy of these parameters. Using a finite element approach may be the only feasible method if no empirical data exists or if the complexity of the problem is too great.

AUTODYN was useful in predicting the behavior of internal reflections that occur with the confined explosions of the JCAT-340 tests. Even though the peak pressures from the FEA models were consistently underestimated, the calculated impulse agreed well with the recorded test data. However, as the charge size increased for the tests, empirical calculations failed to predict the large pressures recorded because of the increasingly chaotic nature of the confined blast.

The effect of secondary reactions in a confined structure depends largely on the oxygen balance of the explosive, the volume of the confining structure, and the venting area. Structures that have a large venting area, such as the Building 340 bays, see a relatively constant effect from the secondary combustion reactions after a critical charge size. The critical charge size relates to the volume of the structure available for the secondary combustion reactions because any additional amount of detonation products generated by the charge will be pushed out of the structure by the expanding gasses. Calculations showed the combustions gasses from 72 lb of PBX-9501 would completely fill a 20-ft-wide bay. However, actual test video showed this occurring with a 50-lb charge.

The methods presented in this thesis for analysis of the secondary combustion reactions could be altered to apply to different scenarios. The focus of the analysis of the JCAT-340 tests was for charges of PBX-9501, but the calculation methods are similar for other explosives. Additionally, fireball size predictions could analyze other consequences of an accidental detonation such as the potential of starting a fire in nearby forest and flora.

APPENDIX A

A. AUTODYN Remap Feature and Parameters Used for Air Blast Models

Many times, including an explosive detonation into a finite-element model for explosively driven events or studying the behavior of a detonation is desirable. To accurately model the detonation process, the finite element method requires a minimum of ten computational cells across the HE material. If the explosive takes up very little space relative to the rest of the model, such as the AUTODYN bay models used for JCAT-340, this requirement results in a model with a very high number of cells and would be computationally inefficient. AUTODYN offers a feature where the initial detonation calculation can be carried out in a separate 1-D or 2-D model and then remapped into a 3-D environment using an axis of symmetry.

Because the remap file originates in 1-D or 2-D geometry, it can contain a large number of elements and provide an accurate detonation model. A spherical explosive charge would use a 1-D "wedge" subgrid that models a small angle of the explosive material for the detonation calculation. This wedge is rotated about two axes to form a sphere when remapped into a 3-D model. Any other axially symmetric explosive geometry can be generated using a 2-D model.

B. Equations of State Used in AUTODYN

After a certain amount of expansion, the Equation of State (EOS) for the gaseous detonation products changes from Jones-Wilkins-Lee (JWL) to the Ideal Gas EOS. The reason for this change is to avoid errors in the computation of the material density, which is calculated by $\rho = \rho_{ref}(+1)$. Because the compression approaches a value of negative one (–1) behind the detonation front, the calculation of density can cause problems. For the JWL EOS, the pressure at constant entropy is given by the following:

$$P = A\left(1 - \frac{\omega}{R_1 V}\right)e^{-R_1 V} + B\left(1 - \frac{\omega}{R_2 V}\right)e^{-R_2 V} + \frac{\omega E}{V} \quad ,$$

where V is a ratio of the volume of detonation products to the volume of undetonated explosive, E is the energy, and A, B, R_1, R_2, and ω are constants specific to the explosive. V increases with expansion so that the exponential terms become negligible. The remainder of this equation is based on the Ideal Gas EOS with corrections. The adiabatic constant, ω, is related to the adiabatic exponent by $\gamma = \omega + 1$. Table A.1 presents an example of the parameters AUTODYN employs for the JWL EOS for PBX-9501.

The JWL EOS is known to be accurate for pressures from detonation product expansions down to 1 kbar.[10] However, the ideal gas law begins to lose accuracy at pressures above 200 bar (~2900 psi).[9] Thus, this region not well covered by either the JWL or Ideal Gas EOS must be kept in mind when choosing the appropriate time to change the equation of state. When changing the EOS, one needs to know what values to use for the density and the adiabatic exponent (i.e., ratio of specific heats). The AUTODYN remap tutorial gave the values for TNT as $\rho = 1 \times 10^{-4}$ g/cm^3 and $\Gamma = 1.35$. Correspondence with Chris Quan at Century Dynamics revealed that this value was

chosen because it is an order of magnitude smaller than standard air density. It is solely a reference value and should be valid to use for other explosives. Fortunately, newer versions of AUTODYN (5.0 and above) have the capability of automatically changing the high-explosive EOS at the appropriate time (when model pressures fall below ~200 bar).

AUTODYN Parameters for PBX-9501	Value	Units
Equation of State	**JWL**	
Reference density	1.83	g/cm^3
Parameter A	8.52E+06	*bar*
Parameter B	1.80E+05	*bar*
Parameter R1	4.55	-
Parameter R2	1.30	-
Parameter W	0.38	-
C-J Detonation velocity	8.78E+02	*cm/ms*
C-J Energy / unit volume	1.02E+05	$kerg/mm^3$
C-J Pressure	3.70E+05	*bar*
Burn on compression fraction	0	-
Pre-burn bulk modulus	0	*bar*
Adiabatic constant	0	-
Auto-convert to Ideal Gas	Yes	
Strength	**None**	
Failure	**None**	
Erosion	**None**	
Material Cutoffs	-	
Maximum Expansion	0.10	-
Minimum Density Factor (Euler)	1.00E-05	-
Minimum Density Factor (SPH)	0.20	-
Maximum Density Factor (SPH)	3.00	-
Minimum Soundspeed	1.00E-06	*cm/ms*
Maximum Soundspeed	1.01E+20	*cm/ms*
Maximum Temperature	1.01E+20	*cm/ms*

Table A.1: AUTODYN parameters for PBX-9501 (JWL EOS).

The ideal gas law can be expressed as $P = \rho RT$. Therefore, for an airblast, the pressure is directly proportional to the air density. This relationship makes it important to

use the correct air density in the Ideal Gas EOS parameters for AUTODYN. The ambient atmospheric pressure can be calculated (psi) at an altitude above MSL by the following:[1]

$$P_0 = 14.6965\left[\frac{288.15}{288.15 - 1.9812\times10^{-3}H}\right]^{-5.25588} \qquad \text{(A.1)}$$

For LANL elevation (7500 ft above MSL), a new value pressure was calculated as P_{atm} = 11.127 psi = 76715 Pa. Assuming a temperature T_{atm} = 288.15 K, the air density was calculated as $\rho_{atm} = 9.276 \times 10^{-4}$ g/cm^3. A corresponding internal energy was also calculated as E = 2068 Merg/g using the ideal gas relationship E = PV/(γ–1) where γ for air is 7/5 (or 1.4). This new density value represents ~25% decrease from the MSL value of P_{atm} = 14.697 psi. If the atmospheric parameters are not changed in the AUTODYN models to account for LANL elevation, AUTODYN overpredicts the pressures and impulse by approximately 5%. Table A.2 shows the AUTODYN parameters for air.

AUTODYN Parameters for Air	Value	Units
Equation of State	**Ideal Gas**	
Reference density	9.28E-04	*g/cm^3*
Gamma	1.40	-
Adiabatic constant	0.00	-
Pressure shift	0.00	*bar*
Reference Temperature	288.20	*K*
Specific Heat	7.18	*Merg/gK*
Strength	**None**	
Failure	**None**	
Erosion	**None**	
Material Cutoffs	-	
Maximum Expansion	0.10	-
Minimum Density Factor (Euler)	1.00E-05	-
Minimum Density Factor (SPH)	0.20	-
Maximum Density Factor (SPH)	3.00	-
Minimum Soundspeed	1.00E-06	*cm/ms*
Maximum Soundspeed	1.01E+20	*cm/ms*
Maximum Temperature	1.01E+20	*cm/ms*

Table A.2: AUTODYN parameters for air (Ideal Gas EOS).

APPENDIX B

General Properties and Parameters for PBX-9501

A. TNT Equivalency Values

The TNT equivalency for PBX-9501 has caused some confusion in the calculations for the JCAT-340 project. An equivalency value is often necessary when scaling empirical data based on charges of TNT or using programs such as BlastX, ConWep, or DDESB-BEC. Fortunately, this confusion is not a concern for AUTODYN models because a JWL EOS is available for PBX-9501 that uses parameters from the *LLNL Explosives Handbook*.[12] Information for the characteristic of PBX-9501 was compiled from several sources and appears in Tables A.3 and A.4.[9,12]

	Weight %	Mole %	Hf [cal/mol]	V/N [cc/mol]	C	H	N	O	MW
HMX	95	92.72	17930	155.47	4	8	8	8	296.2
Estane	2.5	3.94	–184820	160.79	10	14.59	0.37	3.42	194.7
BDNPF	2.5	3.34	–142700	225.96	7.5	13	4	10	319.2
				Total =	4.353	8.427	7.566	7.886	**292.9**

Table A.3: Constituents of PBX-9501 and calculation of the molecular weight.

Material Property	Value for PBX-9501
Molecular Weight, MW	292.9 g/mol
Density, ρ	1.84 g/cm^3 (nominal) 1.833 ±0.005g/cm^3 (pressed)
Detonation Velocity, D	8780 m/s
Heat of Detonation, ΔH_d	–1.32 kcal/g = 1624 kJ/mol
Heat of Combustion, ΔH_c	–2.24 kcal/g = 2748 kJ/mol
$\Delta H_{AB} = \Delta H_c - \Delta H_d$	–0.92 kcal/g = 1124 kJ/mol

Table A.4: Properties of PBX-9501.

The heat of detonation in Table A.4 has been calculated assuming the water in the detonation products is a liquid. Two methods are commonly used for finding TNT equivalence. The first [Equation (A.2)] is based on the energy contained in the explosive relative to TNT. The second method [Equation (A.3)] is known as the "Berthelot Method."[9,14]

$$TNT_{equiv.} = \frac{E_{HE}}{E_{TNT}} = \frac{D_{HE}^2}{D_{TNT}^2} = \frac{D_{HE}^2}{48.3} \qquad \text{(A.2)} \qquad TNT_{equiv.} = 840 * \frac{n_{gas}}{n_{HE}} * \frac{\Delta H_R^0}{MW^2} \qquad \text{(A.3)}$$

For the Berthelot Method, ΔH_R can be either the molar heat of detonation or combustion (in kJ/mol) depending on the desired application. This older method was calibrated using nitroglycerine.

It is apparent that the TNT equivalency of PBX-9501 is not a definite value. Using a scaling factor based on the particular explosive application is recommended. For example, if the concern is for pressures from an airblast, a pressure equivalency method should be used. For example, for the explosive PBX-9404, which has a composition

similar to PBX-9501 but contains 94% HMX, the TIC-11268 gives pressure equivalencies of

TNTeq = 1.13 for pressures of 5–30psi

TNTeq = 1.70 for pressures of 100–1000psi

This reference also notes that if information is limited "a TNT equivalency of 1.3 will generally provide a reasonable and conservative estimate of the TNT charge weight for any high explosive."[1] Using Equation (A.2) gives a TNT equivalency of ~1.6, which seems high compared with the previous statement. The work in this thesis uses the value of 1.129 as given by Appendix A of the TIC-11268.

B. Calculation of Secondary Reaction Extent (Fireball Size):

CHEETAH calculated the detonation reaction for PBX-9501. With only the major (molar fraction ≥ 3%) constituents considered, the reaction can be written as the following:

$$C_{4.353}H_{8.427}N_{7.566}O_{7.886} \overset{\text{Det.}}{\Rightarrow} 3.76N_2 + 2.9H_2O + 1.67CO_2 + 1.63CO + 0.43H_2 + 0.34CH_4$$

These detonation products are assumed to completely combust in air composed of 21% O_2 and 79% N_2 to form H_2O and CO_2. This assumption results in the following:

$$3.76N_2 + 2.9H_2O + 1.67CO_2 + 1.63CO + 0.43H_2 + 0.34CH_4 + 1.71O_2 + 3.87N_2$$
$$\overset{\text{Comb.}}{\Rightarrow} 10.19N_2 + 4.01H_2O + 3.64CO_2$$

The additional 3.87 moles of nitrogen that appears on the left-hand side represent the atmospheric nitrogen in the air that combusts with the detonation products. From this, we calculate the total amount of detonation and combustion product gasses per mole of high explosive.

$$\frac{n_{DG}}{n_{HE}} = 10.73 \qquad \text{and} \qquad \frac{n_{CG}}{n_{HE}} = 10.19 + 4.01 + 3.64 = 17.84$$

This result can determine the molar fraction of each constituent so that a molar averaged heat capacity of the form $C_p = a + bT + cT^2$ can be found for the gasses. Table A.5 shows the results of these calculations.

Constituent	mol gas / mol HE	xi	a	b [10^{-3}]	c [10^{-6}]
N_2	10.190	0.571	6.457	1.389	–0.069
H_2O	4.010	0.225	7.136	2.640	0.046
CO_2	3.640	0.204	6.339	10.140	–3.415
Total =	*17.840*	***Mole Avg. =***	*6.5855*	*3.4557*	*–0.7259*

Table A.5: Molar heat capacity coefficients for combustion gasses.

The additional heat liberated by the combustion process, i.e., the heat of afterburn for PBX-9501, will go into heating the combustion gasses. Using Equation (6-4),

$$2.685 \times 10^5 \frac{cal}{mol} = 17.84 \frac{mol\ gas}{mol\ HE}$$

$$\times \left[6.5855(T_a - 298) + \frac{3.4557 \times 10^{-3}}{2}\left(T_a^2 - 298^2\right) + \frac{-0.7259 \times 10^{-6}}{3}\left(T_a^3 - 298^3\right) \right] \frac{cal}{mol}$$

This calculation gives a calculated temperature of 1906 K, which can be used in Equation (6-5) to give the fireball diameter in feet [after evaluating Equation (6-6)].

$$n_{CG} = \frac{W_{HE}\, 453.59\, {}^{g}\!/_{lb}}{292.882\, {}^{g}\!/_{mol}} \left[10.73 + \frac{10.71}{0.21} \right] = 29.23 W_{HE}$$

$$D = \left(\frac{6}{\pi} \frac{29.23 W_{HE} mol \cdot 0.0820578\, {}^{L \cdot atm}\!/_{mol \cdot K} \cdot 1906 K}{1 atm} \right)^{1/3} \times \frac{10}{30.48} \frac{ft}{L^{1/3}} = 6.756 W^{1/3}$$

$$D = 6.756 \times W^{1/3}$$

R is universal gas constant, 0.0820578 L-atm/mol-K, T is temperature in [K], and pressure, P, is 1 atm.

APPENDIX C

ADDITIONAL ANALYSIS OF JCAT-340 TEST DATA

This section presents additional data from the JCAT-340 tests and comparisons to AUTODYN models not covered in the main manuscript. The data presented here is an addendum to Section 7.0. The conditions for analysis made in that section apply here as well: the actual charge dimensions, atmospheric conditions, and building dimensions were used, and all charges were initiated at the end-facing ceiling.

A. Tests with Blow-Out Panels in Place

As discussed in Section 2.1, the blow-out panels were still in place for the first few tests in Building 340. The blow-out panel requires a finite amount of time to accelerate because of its inertia, and consequently a few shocks are reflected off the panel before the gasses can be vented. This reflection influences the propagation of shocks into the rest of the building and causes the pressures in the adjacent bay hallway to be higher than if the panels were initially removed.

1. 25-LB TEST AND MODEL DATA

Data from this test is presented in Section 7.0.

2. 75-LB TEST AND MODEL DATA

The airblast behavior of the 75-lb shot was very similar to the 25-lb shot. The simulated removal of the blow-out panels in this AUTODYN model occurred at 9 ms. The one-meter charge height for the 25-lb and 75-lb tests resulted in a large amount of

shock reflection off the floor. This reflection caused differences in the shock wave profiles and airblast phenomena between the two charge heights and was probably the cause of the double peak seen during the first pressure pulse of the JCAT test data (see Figure A.1). This feature is also noticeable in the 25-lb test, but is less apparent.

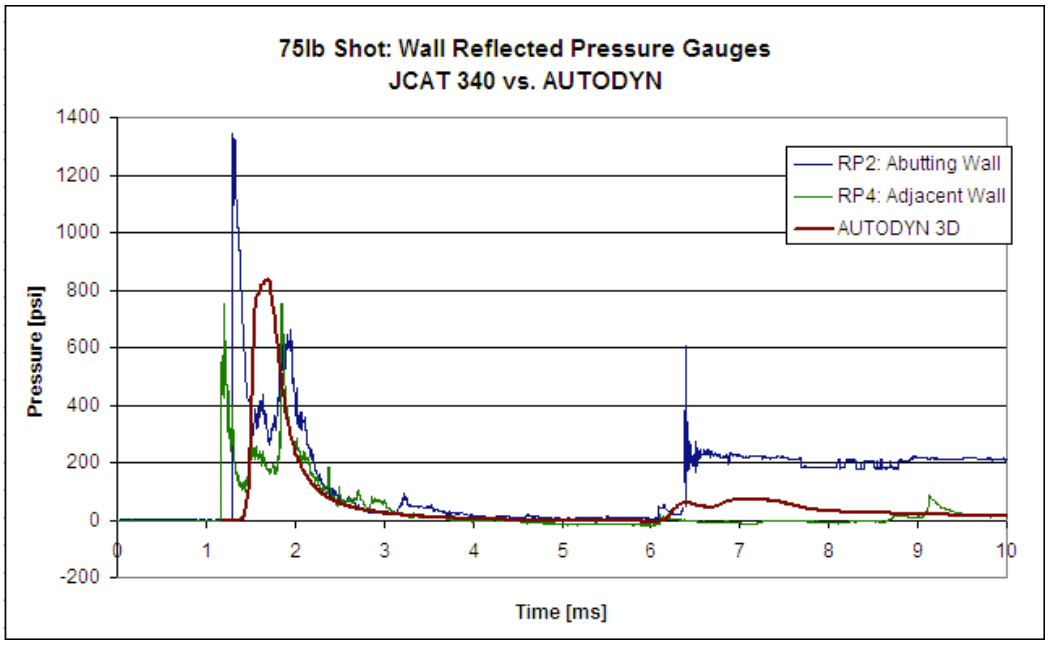

Figure A.1: Experimental and predicted pressure data comparison for the 75-lb test.

Figure A.1 shows a pressure spike that occurred after 6 ms on the abutting wall gauge that caused the pressures to be recorded at an offset value for the remaining time. It is possible that this reading was the result of a fragment or debris hitting the gauge.

The back wall gauge was able to record the entire late-time impulse that occurred from 30 ms to 300 ms (I = 10,644 psi-ms for this time period), but the remaining gauges did not record the entire event. The adjacent wall gauge recorded about half of the event until it was clipped at 127 ms.

B. Tests with Blow-Out Panels Removed

Most of the tests with charge size larger than 1 lb were performed with the blow-out panels missing from Building 340. For the center-bay charge location tests, these are the 5-lb, 50-lb, and 100-lb shots.

1. 5-LB TEST AND MODEL DATA

The first 5-lb center-bay shot located 2 m × 2 m from the left back corner of the bay removed the blow-out panel. For this small charge size, the AUTODYN predictions agree well with the test data (see Figure A.2). The abutting wall gauge recorded a double peak similar to the previous tests described, and the shock time of arrival was slightly ahead of the adjacent wall. Asymmetry in the charge detonation was likely the cause of these differences.

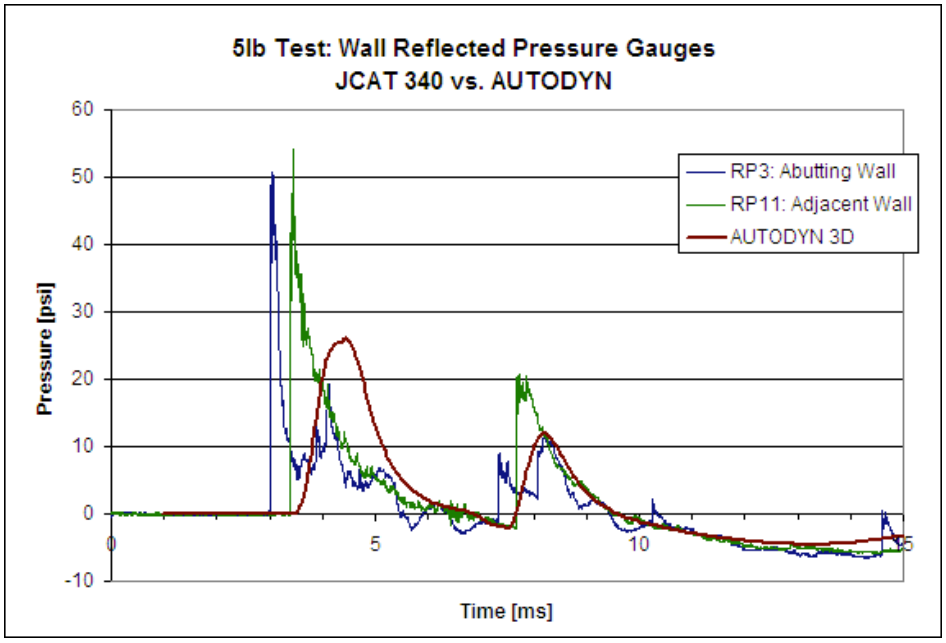

Figure A.2: Experimental and predicted pressure data comparison for the 5-lb test.

2. 50-LB TEST AND MODEL DATA

A single data point from the adjacent wall gauge was removed for this analysis because it seemed inconsistent with the data and peak pressure profiles obtained from the other tests. This point was previously the largest pressure recorded and caused the peak pressure to drop from 1154 psi to 781psi. AUTODYN predicts a distinct second peak from the floor reflection, which is difficult to detect in the test data shown in Figure A.3.

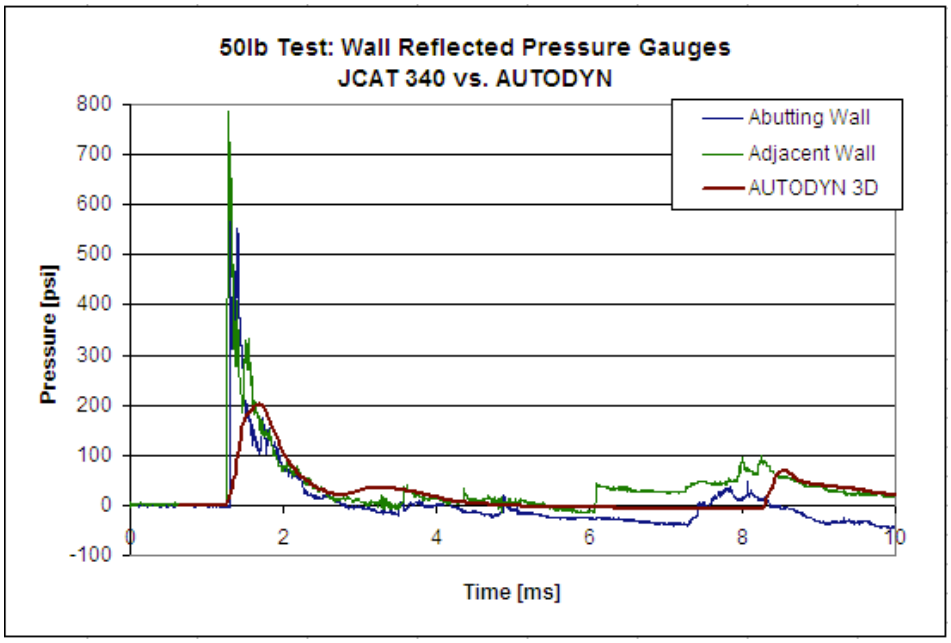

Figure A.3: Experimental and predicted pressure data comparison for the 50-lb test.

The predicted and actual ceiling center pressures were higher than all other gauges analyzed for this test (see Figure A.4). The 50-lb charge had an L/D ratio of 0.50, which was the lowest of all the tests. For L/D ratios of less than one and at scaled distances less than ~12 ft/lb$^{1/3}$, the pressures at the detonator end of the charge, $\theta = 180^{o}$, were at a maximum.[1] In this case, Z = 3.77 ft/lb$^{1/3}$ (Table 3), and the pressures here were larger than at any other angle around the charge. For more information, refer to the analysis presented in Section 4.3.

The high-speed video for the 50-lb test again captured the black column of detonation products seen Figure 30 for the 5-lb test that jets towards the ceiling. The video for this shot showed the detonation products being ignited by the shock reflecting off the ceiling and combining with the combustion front traveling from below. This combustion process would cause a large amount of heat and pressure to develop in the area of the center ceiling gauge and explains the large pressures recorded. This gauge quickly started recording incorrect pressures (after ~3.2 ms).

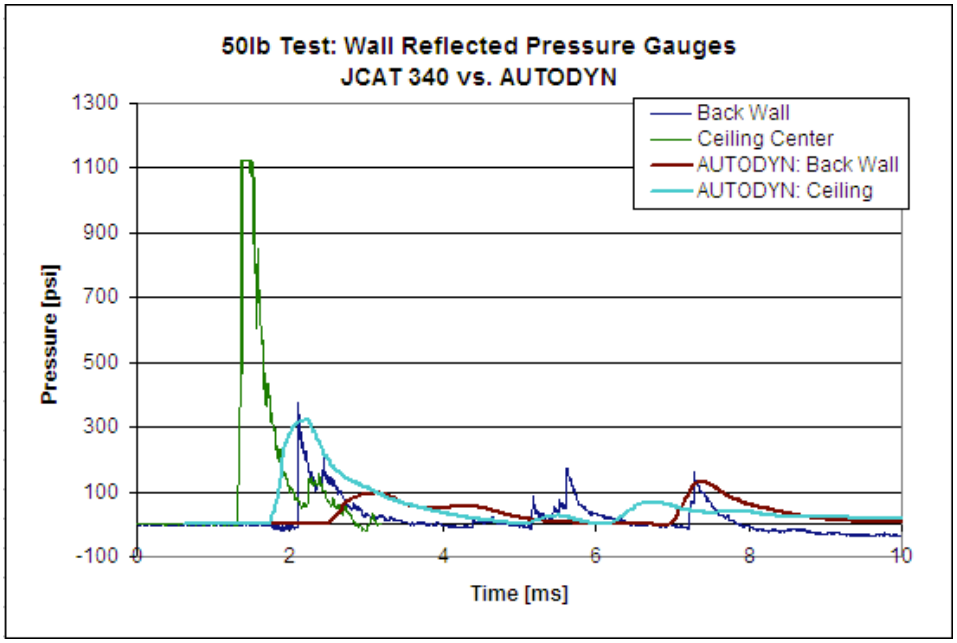

Figure A.4: Back wall and ceiling pressure data comparison for the 50-lb test.

A large late-time impulse was partially recorded by all but the ceiling gauges, but none succeeded in capturing the entire event. The impulse occurred between 20 ms and 250 ms with pressures reaching values of 90 psi.

3. 100-LB TEST AND MODEL DATA

The peak pressures obtained from the 100-lb test data represent the furthest deviation from the ATUDOYN predicted pressures. This large charge size would likely facilitate the formation of a large amount of debris and fragments that could disrupt or harm the gauges and test equipment. Additionally, the secondary effects seen in the previous smaller tests would be exaggerated for the 100-lb charge. The data presented in Figure A.5 shows both the entire pressure range and a more detailed plot that has been reduced by an order of magnitude.

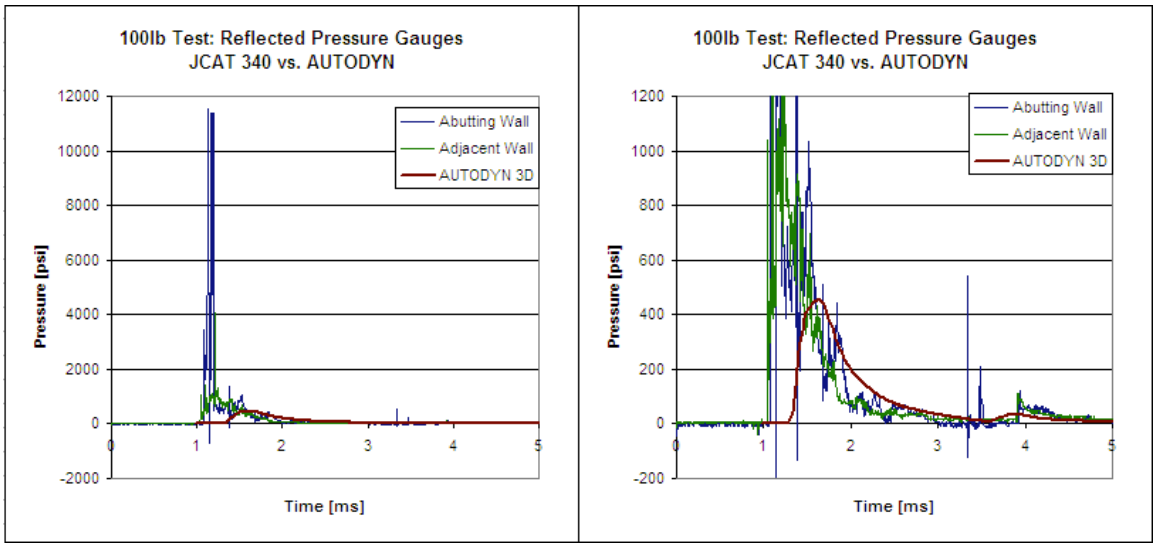

Figure A.5: Experimental and predicted pressure data comparison for the 50-lb test.

The abutting wall gauge was the only gauge to correctly capture the late-time impulse. The adjacent wall gauge jumped to artificially high values, and the back wall gauge fell to unreasonable negative pressures. The impulse for the abutting wall gauge is shown in Figure A.6 and lasts from ~30 ms to 300 ms. The total positive impulse calculated over the time range was 10,616 psi-ms.

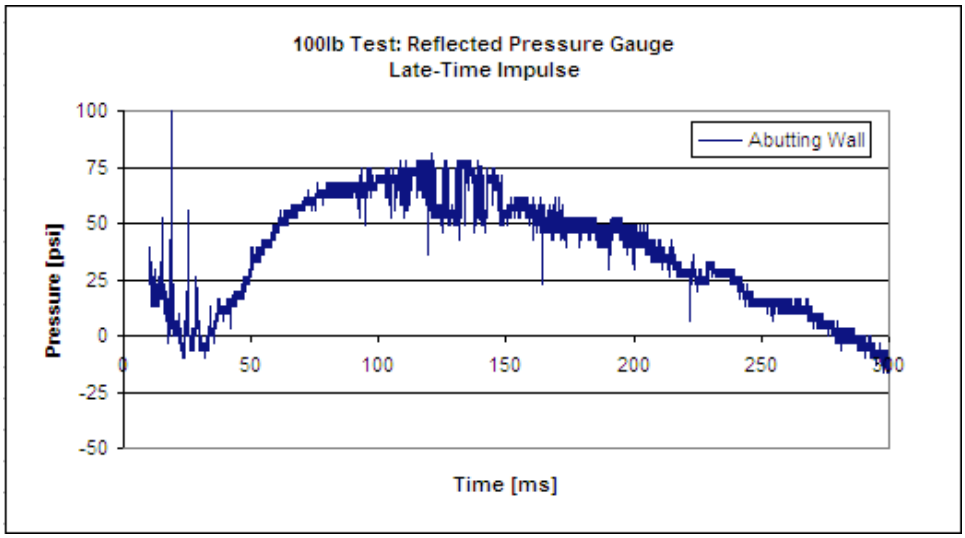

Figure A.6: Pressures from 10 ms to 300 ms for the 100-lb shot.

REFERENCES

1. Baker, W.E., J.J. Kulesz, P.S. Westine, P.A. Cox, and J.S. Wilbeck. *A Manual for the Prediction of Blast and Fragment Loadings on Structures.* U.S. Department of Energy, Albuquerque Operations Office, Amarillo Area Office, Pantex Plant. DOE/TIC-11268 (November 1980).

2. Powell, S.J., and K.A. Steinhaus. "High-Explosives Engineering Training Program (HEET)." (August 29, 2002).

3. Anderson, C.A. "Internal Blast Loading of Scale-Model Explosive-Processing Bay." Los Alamos Scientific Laboratory Report LA-4145 (July 1969).

4. Del Frate, R. SAIC. Private communication (2004).

5. PCB Group. "PCB Piezotronics Model 101A." <www.pcb.com/spec_sheet.asp?model=101A&item_id=955> 1999.

6. PCB Piezotronics, Inc. "PFS: Pressure Catalog." Piezoelectric Sensors for Dynamic Pressure Measurements. <www.pcb.com>. (Depew, New York 2004).

7. Meyers, M.A. *Dynamic Behavior of Materials. (*John Wiley & Sons, Inc., New York, 1994).

8. Akhavan, J. *The Chemistry of Explosives.* (RSC Paperbacks, Cambridge, UK, 2001).

9. Cooper, P.W. *Explosives Engineering. (*Wiley-VCH, New York, 1996).

10. Century Dynamics, Inc. "Theory Manual. Rev. 4.3." AUTODYN Documentation, California, 2003.

11. Fickett, W., and W.C. Davis. *Detonation: Theory and Experiment.* (Dover Publications, Inc., Mineola, New York, 1979).

12. Dobratz, B.M, and P.C. Crawford. *LLNL Explosives Handbook.* UCRL-52997 Rev. 2 (January 1985).

13. Zukas, J.A., and W.P. Walters, Eds. *Explosive Effects and Applications.* (Springer-Verlag, New York, 1998).

14. Kinney, G.F. *Explosive Shocks in Air.* (Macmillan, New York, 1963).

15. Baker, W.E. *Explosions in Air.* (University of Texas Press, Austin, TX, 1973).

16. Kingery, C.N., and G. Bulmash. *Airblast Parameters from TNT Spherical Air Burst and Hemispherical Surface Burst.* U.S. Army Ballistic Research Laboratory, ARDC, Aberdeen Proving Ground, MD. ARBRL-TR-02555 (April 1984).

17. Science Application International Corporation. “BlastX Help.” BlastX v 4.2. U.S. Army Engineer Research and Development Center, Geotechnical and Structures Laboratory (April 2001).

18. Hyde, D. *ConWep 2.1.0.1.* U.S. Army Engineer Research and Development Center, Geotechnical and Structures Laboratory (2003).

19. Swisdak, M.M., Jr., and. J.M. Ward. “DDESB Blast Effects Computer Version 5.0.” Excel macro program (August 2001).

20. Von Neumann, J., and R.D Richtmyer. “A Method for the Numerical Calculation of Hydrodynamic Shocks,” *Journal of Applied Physics* Vol. **21,** 232–239 (1950).

21. Swisdak, M.M., Jr. *Explosion Effects and Properties: Part I – Explosion Effects in Air.* Naval Surface Weapons Center. White Oak Laboratory. NSWC/WOL/TR 75-116 (October 1975).

22. Fertis, D.G. *Mechanical and Structural Vibrations.* (John Wiley & Sons, Inc., New York 1995).

23. Wilke, J.P. Private communication (2004).

24. Kuhl, A.L., R.E. Ferguson, R. Spektor, and A.K. Oppenheim. “Combustion of TNT Products in a Confined Explosion” (17th International Colloquium on Dynamics of Explosions and Reactive Systems, Heidelberg, Germany, July 25–30, 1999).

25. Fried, L.E., W.M. Howard, and P.C. Souers. “Cheetah 4.0 User’s Manual.” Lawrence Livermore National Laboratory, Energetic Materials Center (2001).

26. Merrifield, R. “Fire and Explosion Hazards to Flora and Fauna from Explosives,” *Journal of Hazardous Materials* **A74**, 149–161 (2000).

27. Merrifield, R., and R.K. Wharton. “Measurement of the Size, Duration, and Thermal Output of Fireballs Produced by a Range of Propellants.” *Propellants, Explosives, Pyrotechnics* **25**, 179–185 (2000).

28. United Kingdom Health and Safety Executive. “HID Safety Report Assessment Guide: Chemical Warehouses – Hazards.” Hazardous Installations Directorate. <www.hse.gov.uk/comah/sragcwh/hazards/haz5.htm> (October 2002).

29. Zel’dovich, Y.B., and Y.P. Raizer. *Physics of Shock Waves and High-Temperature Hydrodynamic Phenomena.* (Dover Publications, New York, 2002).

30. PCB Piezotronics, Inc. “Introduction to Piezoelectric Pressure Sensors.” PCB Tech Support. <http://www.pcb.com/techsupport/tech_pres.aspx> (2000).


Los Alamos
NATIONAL LABORATORY
EST.1943